

CNO dredge-up in a sample of APOGEE/Kepler red giants: Tests of stellar models and Galactic evolutionary trends of N/O and C/N

Fiorenzo Vincenzo¹★ David H. Weinberg^{1,2}, Josefina Montalbán³, Andrea Miglio^{4,5,3}, Saniya Khan³, Emily J. Griffith¹, Sten Hasselquist^{6,7}, James W. Johnson¹, Jennifer A. Johnson¹, Christian Nitschelm⁸, Marc H. Pinsonneault¹

¹Department of Astronomy & Center for Cosmology and AstroParticle Physics, The Ohio State University, Columbus, OH 43210, USA

²Institute for Advanced Study, Princeton, NJ 08540, USA

³School of Physics and Astronomy, University of Birmingham, Edgbaston, B15 2TT, UK

⁴Dipartimento di Fisica e Astronomia, Università degli Studi di Bologna, Via Gobetti 93/2, I-40129 Bologna, Italy

⁵INAF – Osservatorio di Astrofisica e Scienza dello Spazio di Bologna, Via Gobetti 93/3, I-40129 Bologna, Italy

⁶Department of Physics & Astronomy, University of Utah, Salt Lake City, UT, 84112, USA

⁷NSF Astronomy and Astrophysics Postdoctoral Fellow

⁸Centro de Astronomía (CITEVA), Universidad de Antofagasta, Avenida Angamos 601, Antofagasta 1270300, Chile

9 June 2021

ABSTRACT

Surface abundances of C, N, and O in red giants are affected by processed material mixed into the stars’ convective envelopes. Using a sample of ~ 5100 stars with elemental abundances from APOGEE and asteroseismic masses from *Kepler*, we test theoretical stellar models that predict this mixing, then apply these models to derive birth C, N, and O abundances for these stars. Our models with standard mixing can reproduce the observed trends to within plausible uncertainties in the birth abundances. Some models with “extra” mixing processes fail, predicting trends with surface gravity or evolutionary state that are not observed. Applying mixing corrections to the APOGEE abundances removes the observed age-dependence of $\log(\text{N/O})$ and $\log(\text{C/N})$, but it leaves trends of $\log(\text{N/O})$ and $\log(\text{C/N})$ with metallicity, as expected based on nucleosynthesis models. The stellar N/O trend agrees well with Dopita et al.’s calibration of gas phase $\log(\text{N/O})$ with metallicity, and with gas phase trends in the MaNGA integral field survey of nearby galaxies. We also find a substantial separation in birth $[\text{N/Mg}]$ ratios between high- $[\alpha/\text{Fe}]$ (“thick disc”) stars and low- $[\alpha/\text{Fe}]$ (“thin disc”) stars. We find a smaller but still clear separation for $[\text{C/Mg}]$. The trends of birth C and N abundances with $[\text{Fe/H}]$ and $[\alpha/\text{Fe}]$ could affect spectroscopic age estimates for red giants that rely on the observed C/N ratio as a diagnostic of stellar mass.

Key words: Galaxy: abundances – stars: general – stars: abundances – stars: evolution – stars: low-mass – stars: atmospheres

1 INTRODUCTION

The working assumption of the majority of chemical evolution studies is that present-day stellar photospheres retain the chemical composition of the molecular clouds from which stars were born. Since the stars within a given volume $\mathcal{V}(x, y, z)$ of the Milky Way (MW) are characterized by a distribution of ages, chemical evolution studies use atmospheric chemical abundances as measured in stars with different ages to constrain the chemical enrichment history of the interstellar medium (ISM) within $\mathcal{V}(x, y, z)$ from different nucleosynthetic sources (e.g., Romano et al. 2010; Mollá et al. 2015;

Prantzos et al. 2018; Kobayashi et al. 2006; Kobayashi, Karakas, & Lugaro 2020).

One complication in interpreting such data is that radial migration of stars may mix populations with different enrichment histories, as pointed out by many observational (e.g., Hayden et al. 2015; Casagrande et al. 2016; Grieves et al. 2018; Miglio et al. 2021) and theoretical works (e.g., Schönrich & Binney 2009; Loebman et al. 2011; Bird, Kazantzidis, & Weinberg 2012; Minchev, Chiappini, & Martig 2013, 2014; Vincenzo & Kobayashi 2020; Johnson et al. 2021). A second complication, and the focus of this paper, is that internal mixing during stellar evolution causes the present-day atmospheric abundances in red giants to differ from their birth abundances, a phenomenon expected theoretically and demonstrated by

★ email: vincenzo.3@osu.edu

observations in open cluster and globular clusters (e.g., Gilroy 1989; Korn et al. 2007; Lind et al. 2008; Souto et al. 2018, 2019).

As stars ascend the red-giant branch (RGB), standard stellar evolution models predict C and N abundances to change at the stellar surface, because the convective envelope reaches increasingly deep regions inside the stars, dredging up material already processed by H-burning during the main sequence (MS). In this process (the so-called *first dredge-up*), the pristine material in the stellar envelope is effectively mixed with processed material coming from the inner layers. The main effect of the first dredge-up is to increase the abundances of ^4He , ^{13}C , and ^{14}N at the stellar surface, whereas ^7Li and ^{12}C are decreased (e.g., see the theoretical works of Iben 1964, 1967; Dearborn, Eggleton, & Schramm 1976; Dearborn, Tinsley, & Schramm 1978, and the observational works of Greene 1969; Lambert & Ries 1977; Kjaergaard et al. 1982; Cottrell & Sneden 1986; Shetrone, Sneden, & Pilachowski 1993; Shetrone et al. 2019).

Because the reaction $^{14}\text{N}(p,\gamma)^{15}\text{O}$ is much slower than other reactions in the CNO cycle, the abundance of ^{14}N is drastically increased in regions of CNO burning, primarily at the expense of ^{12}C . In stars with increasing mass, the convective envelope during the RGB dredges up increasing amounts of CNO-processed material from regions where H was partly but not completely burned to helium on the MS. For this reason, the decrease of $\log(\text{C}/\text{N})$ and the increase of $\log(\text{N}/\text{O})$ in the stellar envelope at the end the first dredge-up correlate with the stellar mass, being larger for stars with higher mass. Because the age of a red giant is essentially determined by the MS lifetime, which is in turn determined by mass, many recent studies have investigated the use of $\log(\text{C}/\text{N})$ or spectral features that respond to C/N as diagnostics of stellar age, empirically calibrated using clusters, asteroseismology, or isochrones (e.g., Masseron & Gilmore 2015; Salaris et al. 2015; Martig et al. 2016; Ness et al. 2016; Casali et al. 2019; Miglio et al. 2021).

By measuring the abundances of Li, C, N, and O in a sample of metal-poor red giants in the field, Gratton et al. (2000) observed a significant depletion of C and Li as well as an enhancement of N after the bump in the RGB luminosity function (see Section 2.3.2 for more details and references). Gratton et al. (2000) concluded that an *extra-mixing process* is needed to explain the observed abundance changes in addition to standard mixing mechanisms such as the first dredge-up, which is experienced by red giants before they move across the RGB bump. Similar conclusions were also drawn by Angelou et al. (2011, 2012, 2015), who observed that the abundances of Li and C in a sample of RGB stars in metal-poor globular clusters are significantly depleted at luminosities above the RGB bump, whereas N is enhanced.

Interestingly, by testing the predictions of models assuming extra-mixing due to thermohaline instability (see Section 2.3.2), Angelou et al. (2015) could reproduce the observed depletion of Li and C as a function of stellar luminosity above the RGB bump; however, fitting the observed relation of Li abundance vs stellar luminosity required a dimensionless parameter for the thermohaline mixing of Li that was a factor of ≈ 5 times lower than that required to fit the observed C vs stellar luminosity relation. More recently, Lagarde et al. (2019) developed stellar population synthesis models showing that the assumption of thermohaline instability could help reproduce the trend of $\log(\text{C}/\text{N})$ vs metallicity as observed in a sample of red giants in the field by the Gaia-ESO survey (GES; Gilmore et al. 2012; Randich, Gilmore, & Gaia-ESO Consortium 2013), as well as the observed trend of $\log(\text{C}/\text{N})$ vs turn-off mass in a sample of red giants in open clusters and globular clusters.

Understanding CNO evolution is important for testing stellar astrophysics, for interpreting results of Galactic chemical evolution

surveys that target red giants, and also for extragalactic studies. Nebular N and O abundances can be measured from the analysis of the emission lines in the spectra of individual HII regions within our Galaxy (e.g., Shaver et al. 1983; Vilchez & Esteban 1996; Aflerbach, Churchwell, & Werner 1997; Rudolph et al. 2006; Fernández-Martín et al. 2017; Esteban & García-Rojas 2018) and extragalactic systems (e.g., Pagel & Edmunds 1981; Garnett & Shields 1987; Berg et al. 2020; Esteban et al. 2020). Statistical samples of N and O abundance measurements in extragalactic systems are also available thanks to large spectroscopic surveys of galaxies in the nearby Universe (e.g. Andrews & Martini 2013; Pérez-Montero et al. 2016; Belfiore et al. 2017; Schaefer et al. 2020). Examples of such surveys are Mapping Nearby Galaxies at Apache Point Observatory (MaNGA; Bundy et al. 2015) and Calar Alto Legacy Integral Field Area (CALIFA; Sánchez et al. 2012). Many studies of the gas-phase metallicities in these integral field surveys and integrated galaxy spectra at low and high redshift make use of strong-line diagnostics based on N/O (e.g., Kewley & Dopita 2002; Pettini & Pagel 2004; Pérez-Montero & Contini 2009; Dopita et al. 2016). This choice is justified by the fact that the nucleosynthesis of N in asymptotic giant-branch (AGB) stars and massive stars strongly depends on metallicity (see Henry, Edmunds, & Köppen 2000; Vincenzo et al. 2016, and references therein), and a tight correlation between N/O and O/H in the ISM of galaxies is observed by several studies (e.g., see the recent work of Berg et al. 2020, and references therein), as well as predicted by cosmological hydrodynamical simulations (e.g., Vincenzo & Kobayashi 2018b). By analysing a sample of star-forming galaxies observed by MaNGA, Schaefer et al. (2020) found that the observed variation of N/O at fixed O/H correlates with the local star formation efficiency, in agreement with the predictions of chemical evolution models (Vincenzo et al. 2016).

In this work, we study how C, N, and O abundances vary in a sample of ~ 5100 red giants observed by the the Apache Point Observatory Galactic Evolution Experiment (APOGEE; Majewski et al. 2017) and the *Kepler* mission (Borucki et al. 2010). From the asteroseismic analysis of the *Kepler* light curves of these stars, Miglio et al. (2021) could accurately constrain their masses and radii. Pinsonneault et al. (2018) carried out a similar effort with APOGEE+*Kepler* stars using different methodology for the asteroseismic modeling. Our paper has three inter-locking goals. First, we use the APOGEE+*Kepler* observations to test the predictions of different stellar evolution models, including either standard mixing predictions or extra-mixing mechanisms (see Section 3). Second, we apply the theoretical mixing corrections to infer the birth C, N, and O abundances of our APOGEE sample, which we use to examine trends of elemental abundance ratios as a diagnostic of chemical enrichment scenarios (see Section 4). Third, recognizing the large uncertainties in empirical metallicity calibrations based on strong emission lines (e.g., Kewley & Ellison 2008), we compare the evolution-corrected N/O vs O/H trend in our red giant sample to gaseous nebulae in the Local Universe to constrain the best metallicity calibration (see Section 5).

2 DATA AND MODELS

The surface abundances of N and C (and to some extent O) in evolved stars differ from their birth abundances because stellar material that has been processed by CNO burning is mixed into the convective envelope. The ratio N/C increases drastically in regions where CNO burning has reset abundances to the equilibrium determined by nuclear reaction rates. In solar core conditions, for

example, the birth ratio $N/C \approx 0.25$ is reset to $N/C \approx 225$. Surface abundances of N and C therefore depend on the fraction of material now in the convective envelope that was once in a zone subject to the CNO cycle. Typically O abundances are little affected because the branch of the CNO cycle involving ^{16}O only comes into play at high temperatures. We consider several different models for mixing in RGB and RC stars, as a function of mass and metallicity. To test these models against data and derive evolution-corrected abundances, we require stars with measured C, N, O surface abundances, overall metallicity, and masses. For this purpose, we use Miglio et al.'s (2021) sample of APOGEE stars with mass estimates based on *Kepler* asteroseismology. In our analysis, chemical abundance measurements are from APOGEE-DR16 (Wilson et al. 2019; Ahumada et al. 2020; Jönsson et al. 2020), which are scaled with respect to the solar abundances as measured by Grevesse, Asplund, & Sauval (2007).

2.1 The sample of red giants of Miglio et al. (2021)

Using a combination of spectroscopic and asteroseismic constraints Miglio et al. (2021) inferred masses, radii, and ages of about 5400 red-giant stars observed by *Kepler* and APOGEE. In this work we adopt stellar parameters resulting from their reference run R1, and refer the reader to their Table 1 and Sec. 2 for a discussion of the systematics that affect the accuracy of the inferred properties, both related to biases in the data and from the grid of stellar models adopted in the modelling code.

From the initial sample of giants we exclude stars with an inferred radius larger than $30 R_{\odot}$ to avoid stars in the poorly-tested low-frequency domain, thus adopting less restrictive criteria than those used in Sec. 4 of Miglio et al. (2021). We obtain a sample of ~ 5100 stars with a median random uncertainty of 6% in mass and of 25% in age.

2.2 The MESA stellar evolution models

This grid of stellar models has been computed using the code MESA (Paxton et al. 2011, 2013, 2015, 2018, version 11532)¹. It covers masses from 0.6 to $3.0 M_{\odot}$ with a step of $0.05 M_{\odot}$ and evolution phases from zero age main sequence (ZAMS) to the first AGB-pulse. Our solar-mixture reference is that from Asplund et al. (2009, AGSS09), and in addition to the solar scaled chemical composition, we also consider α -element enhancement of 0.2 and 0.4 dex^2 . For each of these reference mixtures we consider eight different values of $[\text{Fe}/\text{H}]$, ranging from -1.50 to $+0.25$. Radiative opacity values for these specific chemical element mixtures come from OPAL opacity tables (Iglesias & Rogers 1996) complemented with tables by the Wichita State University for the low-temperature domain (Ferguson et al. 2005). Nuclear reaction rates are from the NACRE compilation (Angulo et al. 1999), and the equation of state is computed with the code FreeEOS (Irwin 2012). Concerning transport process, we adopt the mixing-length formalism of convection (Böhm-Vitense 1958) with a mixing-length parameter derived from solar calibration with the same physics, which is kept fixed for the whole grid. These models also include the effects of gravitational settling following the approach by Thoul, Bahcall, & Loeb (1994), with the efficiency

of microscopic diffusion slightly decreased by including a turbulent diffusion term (Morel & Thévenin 2002).

Concerning chemical mixture at the border of convection regions, we do not consider extra-mixing at the limit of the convective core in H-burning MS stars. Assuming a diffusive convective core overshooting has a negligible effect on the predictions of our models for stars with initial mass $m \lesssim 2 M_{\odot}$; for stars with mass $m \gtrsim 2 M_{\odot}$, increasing the convective core overshooting efficiency, $f_{\text{ov,core}}$, from 0 to 0.02 causes a further enhancement of the predicted N abundances at the end of the first dredge up by $\approx 0.04 \text{ dex}$. For the central He-burning phase, we adopt the Bossini et al. (2015) formalism, in which extra-mixing is allowed at the limit defined by Schwarzschild criterion and whose extension has been checked against the AGB-bump location. Finally, we also assume a diffusive extra-mixing at the bottom of the convective envelope, following the parametrisation by Herwig et al. (1997), with an overshooting parameter $f_{\text{ov}} = 0.02$ (Khan et al. 2018). Khan et al. (2018) found that models with higher f_{ov} at low metallicities could better reproduce the position of the RGB bump; in this paper, we do not modify the value of f_{ov} for different metallicity models. We find that increasing f_{ov} from 0.02 to 0.05 causes a further increase of $\log(N/H)$ at the end of the first dredge up by ≈ 0.03 in stars with mass $m = 1 M_{\odot}$, regardless of their metallicity, whereas it does not affect the predicted surface abundances of stars with mass $m > 1 M_{\odot}$.

2.3 The stellar evolution models of Lagarde et al. (2012) with rotation-induced mixing and thermohaline instability

2.3.1 Rotation-induced mixing

If stars have non-negligible rotation on the zero-age main sequence, the dynamical evolution of their angular momentum in the radiative regions is governed by an advection-diffusion partial differential equation (e.g., see Zahn 1992; Maeder & Zahn 1998, and equation 4 of Lagarde et al. 2012); the spatial derivatives in this equation are associated to angular momentum transport mechanisms, which correspond to (i) meridional circulation (advection term, inducing differential rotation) and (ii) shear-induced turbulence (diffusion term, inducing uniform rotation).

The meridional circulation and shear turbulence mechanisms governing the angular momentum transport induced by rotation cause - together with microscopic diffusion - a vertical transport of chemical elements in the radiative regions of the stars (Chaboyer & Zahn 1992; Charbonnel, Vauclair, & Zahn 1992; Chaboyer, Demarque, & Pinsonneault 1995; Decressin et al. 2009b) which can be treated as a diffusion process, simplifying the equations governing the dynamical evolution of the concentration of the chemical elements in stellar evolution models (e.g., see Chaboyer & Zahn 1992; Charbonnel 1995, and equation 5 of Lagarde et al. 2012).

2.3.2 Thermohaline instability

Another proposed mixing process in the radiative regions of red giants - which can effectively alter their surface abundance composition - is the thermohaline instability, which is a double-diffusive process (see Eggleton, Dearborn, & Lattanzio 2006; Charbonnel & Zahn 2007; Charbonnel & Lagarde 2010; Cantiello & Langer 2010, and the recent review of Garaud 2021). Thermohaline instability is predicted to take place after the bump in the luminosity function of RGB stars (Thomas 1967; Iben 1968). In summary, the RGB bump happens after the first dredge-up has reached its deepest extent and the hydrogen-burning shell advances in mass until it interacts with

¹ The code MESA and the relevant documentation are publicly available at the following link: <http://mesa.sourceforge.net>.

² In the MESA stellar evolution models, the α -elements include the following chemical elements: O, Ne, Mg, Si, S, Ar, Ca and Ti.

the H abundance discontinuity, which has been left behind by the withdrawing convective envelope, at the interface between the radiative region and the deepest point of the convective region. When reaching the discontinuity, the mean molecular weight, μ , decreases, causing a sudden decrease of the stellar luminosity for a short period ($L \propto \mu^{7.5}$; e.g., see Schwarzschild 1958).

After the bump in the luminosity function, the hydrogen burning shell advances further through a region which has been homogenized by the convective envelope, where there is a gradient $d \ln \mu / d \ln P$ in the mean molecular weight, μ , with respect to the pressure, P . It is at this time that thermohaline instability is predicted to take place in the radiative region, being induced by an inversion of $d \ln \mu / d \ln P$, due to the thermonuclear reaction ${}^3\text{He}({}^3\text{He}, 2p){}^4\text{He}$ in the outermost layers of the H-burning shell. This reaction can lower the mean molecular weight in a medium which has been chemically homogenized by the first dredge-up, creating lighter fluid parcels which can quickly diffuse to the surface.

Thermohaline mixing is included in stellar evolution models by adding an additional diffusion term in the equation for the dynamical evolution of the concentration of the chemical elements (e.g., see equation 5 of Lagarde et al. 2012). Because of the difficulty of developing high-resolution 3-D models to study in detail this double-diffusive mechanism in stars, the formulation adopted by stellar evolution models like those of Lagarde et al. (2012) leads to a mixing efficiency parameter for thermohaline instability that has been disputed by other numerical experiments based on 2-D models, which find an equivalent efficiency parameter ≈ 10 times lower (e.g., see Denissenkov 2010; Denissenkov & Merryfield 2011, and the discussions in Angelou et al. 2015; Shetrone et al. 2019, and Section 3.6 of Garaud 2021).

2.3.3 The models of Lagarde et al. (2012)

To test the impact of rotation-induced mixing and thermohaline instability on the evolution of the atmospheric chemical abundances in the red giants of our sample, we analyse the predictions of the grid of models as developed by Lagarde et al. (2012) by making use of the Grenoble stellar evolution code (STAREVOL; see Siess, Dufour, & Forestini 2000; Palacios et al. 2003, 2006; Decressin et al. 2009a). Lagarde et al. (2012) also provide a grid of stellar models with standard mixing prescriptions (i.e., no mixing processes are assumed to take place outside of the convective regions), which are used to validate the predictions of the models with extra-mixing prescriptions.

In our analysis, we consider both the models with extra-mixing processes and the models with standard mixing prescriptions. Both grids are computed for initial masses in the range $0.85 \leq m \leq 6 M_{\odot}$ and the following metallicities: $Z = 10^{-4}$, 2×10^{-3} , 4×10^{-3} , and 0.014^3 .

3 TESTS OF EVOLUTIONARY MIXING MODELS

Fig. 1 shows the Kiel diagram with the red giants in the sample of Miglio et al. (2021, red points). The different panels contain stars in different ranges of $[\text{Fe}/\text{H}]$ abundances, centered – from top to bottom – at $[\text{Fe}/\text{H}] = -0.25$, 0.0 , and 0.25 dex. To understand

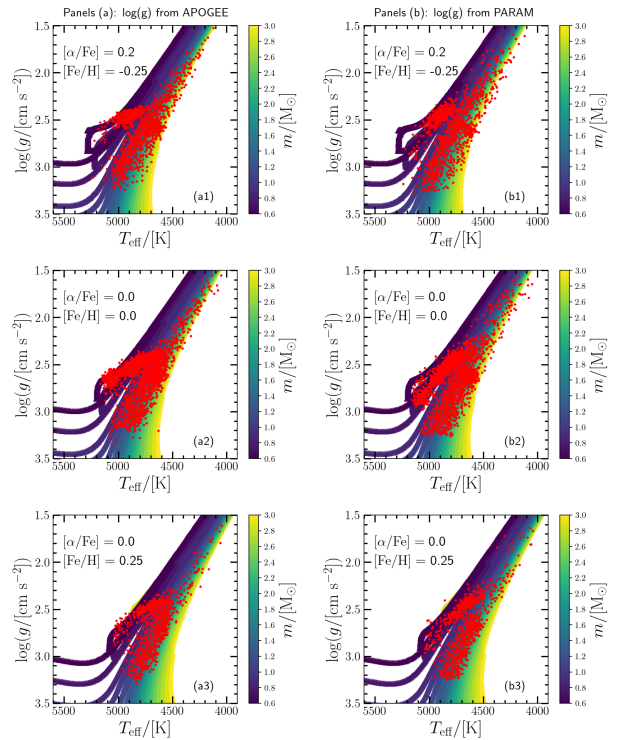


Figure 1. The Kiel diagram with the red giants in the sample of Miglio et al. (2021, red points) as compared with the predictions of our reference MESA stellar evolution models for different stellar masses (color-coding). The stellar models have the $[\alpha/\text{Fe}]$ and $[\text{Fe}/\text{H}]$ abundances reported in the top left corner of each panel. From top to bottom, stars are shown in different bins of $[\text{Fe}/\text{H}]$ with width $\Delta[\text{Fe}/\text{H}] = 0.25$, centered at the value reported in the top left corner. To understand the impact of the systematics in the measurement of $\log(g)$ with different methods, in panels (a1-a3) we use the spectroscopic $\log(g)$ values from APOGEE-DR16, whereas in panels (b1-b3) we use the asteroseismic $\log(g)$ values.

the impact of the systematics in the measurement of $\log(g)$ with different methods, the stars in the Kiel diagrams in Fig. 1(a1-a3) have spectroscopic $\log(g)$ values measured by APOGEE-DR16, whereas the stars in Fig. 1(b1-b3) have asteroseismic $\log(g)$ values that we computed from the stellar radii and masses as derived by PARAM (da Silva et al. 2006; Rodrigues et al. 2014, 2017)⁴. The main effects of asteroseismic vs spectroscopic $\log(g)$ values are in the apparent morphology and $\log(g)$ distribution of RC stars, as well as in the spread at low $\log(g)$ above the RC, in the region populated by upper RGB and AGB stars. Since most of the red giants in our sample are post dredge-up or in the RC, and there are few stars with low $\log(g)$, the predicted evolutionary abundance corrections are insensitive to $\log(g)$ at fixed stellar mass, so these differences do not affect our analysis except to the extent that they affect the APOGEE estimates of surface abundances.

In Fig. 1, we also show the stellar evolutionary tracks we computed with MESA (Paxton et al. 2011, 2013, 2015, 2018). Models with $[\alpha/\text{Fe}] = 0$ are adopted in the $[\text{Fe}/\text{H}]$ -bins centered at $[\text{Fe}/\text{H}] = 0.0$ and 0.25 dex, whereas models with $[\alpha/\text{Fe}] = 0.2$ are shown in the bin centered at $[\text{Fe}/\text{H}] = -0.25$, to reflect the observed decrease of $[\alpha/\text{Fe}]$ as the metallicity increases. We note that the

³ The grids of stellar models of Lagarde et al. (2012) can be downloaded at the following link: <https://vizier.u-strasbg.fr/viz-bin/VizieR?-source=J/A+A/543/A108>.

⁴ The web interface of PARAM with the relevant documentation is available at the following link: <http://stev.oapd.inaf.it/cgi-bin/param>.

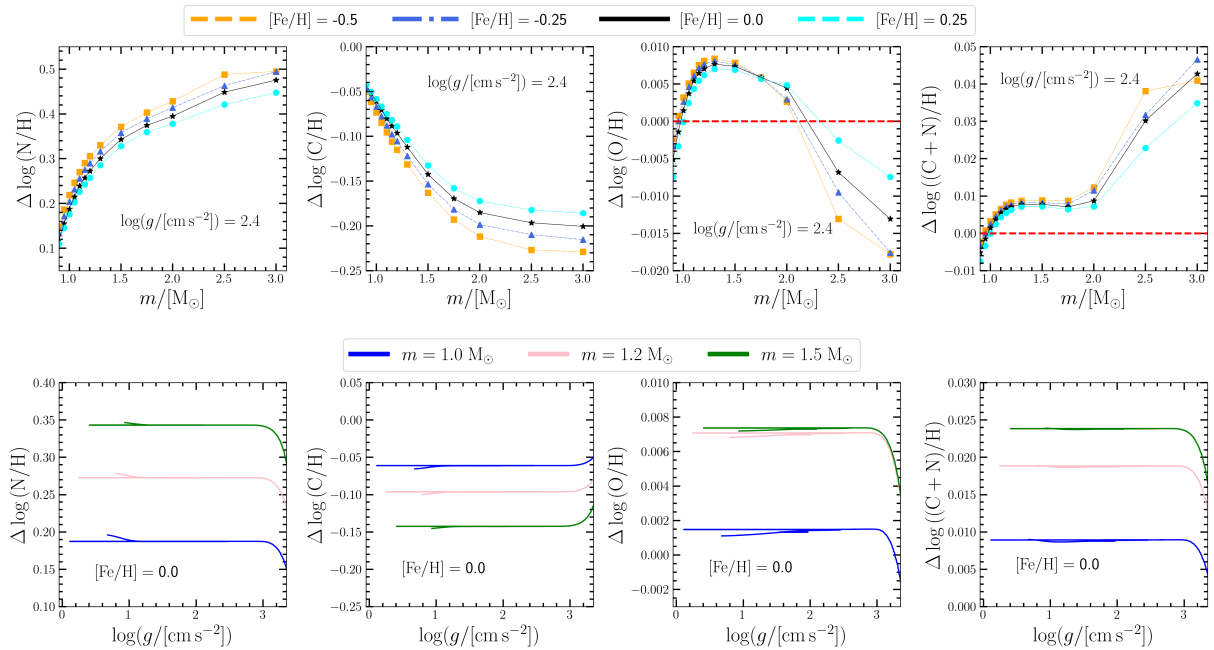


Figure 2. The surface abundance variations $\Delta \log(N/H)$, $\Delta \log(C/H)$, $\Delta \log(O/H)$, $\Delta \log((C+N)/H)$ as predicted by our reference MESA stellar evolution models with respect to the assumed birth abundances. The top panels show the predicted trends vs stellar mass, for different metallicities (orange dashed curves and squares: $[\text{Fe}/\text{H}] = -0.5$; blue dashed-dotted lines and triangles: $[\text{Fe}/\text{H}] = -0.25$; black solid line and star symbols: $[\text{Fe}/\text{H}] = 0$; cyan dashed lines and circles: $[\text{Fe}/\text{H}] = 0.25$), whereas the bottom panels show the predicted trends vs $\log(g)$ for different assumed stellar masses (blue solid lines: $m = 1 M_{\odot}$; pink solid lines: $m = 1.2 M_{\odot}$; green solid lines: $m = 1.5 M_{\odot}$).

models are plotted in order of decreasing stellar mass and lower mass tracks can cover over the tracks of more massive stars. At fixed $[\text{Fe}/\text{H}]$, increasing $[\alpha/\text{Fe}]$ moves the models to lower effective temperatures, improving the agreement with the observations at low $[\text{Fe}/\text{H}]$. Fig. 1 shows that our models can qualitatively explain the observed distribution of stars in the Kiel diagram.

The main uncertainty affecting the evolutionary tracks in Fig. 1 resides in the predicted effective temperatures of the models, which are known to be affected by systematic uncertainty, mostly due to the assumed atmosphere boundary condition and treatment of super-adiabatic convection (Montalbán et al. 2001; Salaris, Cassisi, & Weiss 2002; Montalbán et al. 2004). For this reason, in our analysis, the surface abundance variations of C, N, and O are characterized by considering the surface gravity and not the effective temperature. In summary, the basic stellar parameters in our analysis, which we use to characterize the properties of each star in the sample from a theoretical point of view, are the $\log(g)$ value, mass, $[\text{Fe}/\text{H}]$ abundance, and $[\alpha/\text{Fe}]$ ratio of the stars.

In Fig. 2, we show the predictions of our MESA stellar evolution models for the evolution of the surface abundances of C, N, and O in red giants. The surface abundance change of an element X , $\Delta \log(X/H)$, between the present-day time t and the birth-time t_{birth} , is defined as follows:

$$\Delta \log \left(\frac{X}{H} \right) \equiv \log \left(\frac{N_X(t)}{N_H(t)} \right) - \log \left(\frac{N_X(t_{\text{birth}})}{N_H(t_{\text{birth}})} \right), \quad (1)$$

where N_X and N_H are the number density of atoms of the X species and hydrogen, respectively.

The top panels of Fig. 2 show how the surface abundances of C, N, O, and C+N are predicted to vary in red giants of different mass by our reference stellar models, for a fixed value of the surface gravity $\log(g/[cm s^{-2}]) = 2.4$. Different curves show the predictions of models assuming different $[\text{Fe}/\text{H}]$ abundances. We

fix birth abundance ratios to solar values as we change $[\text{Fe}/\text{H}]$. In our analysis, we adopt a single value of $\log(g)$, because the surface gravity is predicted to have little effect on the surface abundance variations of C, N, O, and C+N among the red giants in our MESA models. This is demonstrated in the bottom panels of Fig. 2, which show how $\Delta \log(X/H)$ for $X = C, N, O$, and C+N change as a function of $\log(g)$ for three different stellar masses ($m = 1, 1.2$, and $1.5 M_{\odot}$), by assuming $[\text{Fe}/\text{H}] = 0$. Similar results are obtained for other stellar masses and metallicities.

The largest changes of the surface abundances are predicted for C and N, whereas the change of O is relatively small, being in the range $-0.02 \lesssim \Delta \log(O/H) \lesssim 0.01$. There is a strong dependence of $\log(C/H)$ and $\log(N/H)$ with stellar mass, such that C is increasingly depleted at the stellar surface as we consider red giants with increasing stellar mass, while N is increasingly enhanced, in agreement with the predictions and results of previous works (e.g., Iben 1964; Casali et al. 2019; Shetrone et al. 2019). For C+N, we find that $\Delta \log((C+N)/H)$ is relatively small among the red giants, being in the range $-0.05 \lesssim \Delta \log((C+N)/H) \lesssim 0.075$, and $0 \lesssim \Delta \log((C+N)/H) \lesssim 0.01$ for $m = 1-2 M_{\odot}$. The near-zero correction arises because extra ^{14}N nuclei are predicted from ^{12}C during CNO processing.

In Fig. 3, we show how $\log(N/O)$ (top panel) and $\log(C/N)$ (bottom panel) change as a function of stellar mass by considering stars classified as RGB by Miglio et al. (2021) with iron abundances in the range $-0.1 \leq [\text{Fe}/\text{H}] \leq 0.1$. The slope of the observed $\log(N/O)$ and $\log(C/N)$ as a function of stellar mass changes at $\approx 1.2 M_{\odot}$, which approximately divides stars with a radiative core in the MS from stars with a convective core. In the same figure, we show the predictions of the stellar models of Lagarde et al. (2012) assuming $Z = Z_{\odot}$ and including either rotation-induced mixing plus thermohaline instability (black solid lines) or standard mixing

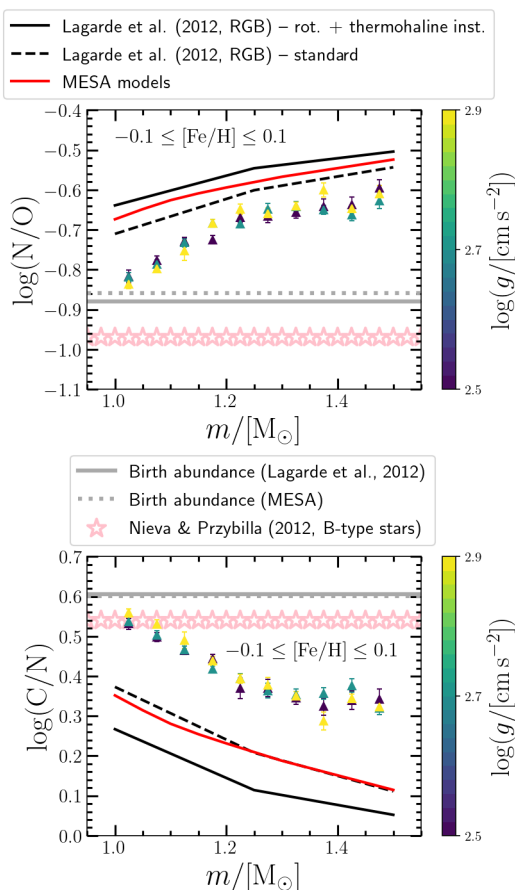


Figure 3. Comparison between the predicted and observed trends of $\log(N/O)$ (top panel) and $\log(C/N)$ (bottom panel) as a function of the stellar mass. The black solid curves correspond to the surface abundances in RGB stars as predicted by the models of Lagarde et al. (2012), assuming rotation-induced mixing and thermohaline instability and metallicity $Z = Z_{\odot}$, whereas the black dashed curves show the models of Lagarde et al. (2012) with standard prescriptions for mixing and $Z = Z_{\odot}$. The red curve shows the prediction of our MESA stellar models for RGB stars assuming $[Fe/H] = 0$. The points with error bars show the observed average trends with corresponding uncertainty on the mean that we measure in the stars classified as RGB by Miglio et al. (2021), by selecting stars with $-0.1 \leq [Fe/H] \leq 0.1$ and different bins of $\log(g/[cm s^{-2}])$ with width of 0.2 centered at the values reported in the color bar. The models assume $\log(g/[cm s^{-2}]) = 2.6$. The gray solid line corresponds to the assumed birth abundances in the stellar models of Lagarde et al. (2012), whereas the gray dotted line shows the assumed birth abundances in our reference MESA models. The pink star symbols show the average abundances in a sample of B-type stars in the Solar neighbourhood as measured by Nieva & Przybilla (2012).

prescriptions similar to our reference models (black dashed lines). We also show the predictions of our reference MESA models (red solid curves), which do not include rotation-induced mixing and thermohaline instability. The birth values of $\log(N/O)$ and $\log(C/N)$ assumed in the models are shown as horizontal gray lines.

In the range of surface gravities spanned by the red giants in our sample, the predicted variation of $\log(N/O)$ and $\log(C/N)$ at stellar fixed mass does not depend on $\log(g)$. For this reason, the model predictions in Fig. 3 are shown as a function of stellar mass by assuming $\log(g/[cm s^{-2}]) = 2.6$. Surface gravity also plays a minor effect in the observed trends of $\log(N/O)$ and $\log(C/N)$ vs stellar

mass among the RGB stars in our sample. When moving from the bin centered at $\log(g/[cm s^{-2}]) = 2.5$ to that at $\log(g/[cm s^{-2}]) = 2.9$, the differences of $\log(N/O)$ and $\log(C/N)$ are below ≈ 0.05 dex for almost all mass-bins, with the exception of RGB stars in the mass-bin $1.35 \leq m < 1.4 M_{\odot}$, which show larger abundance differences. We note that the error bars in Fig. 3 correspond to the uncertainty on the mean.

A difference in the surface abundances between RGB and RC stars of the same mass and metallicity is predicted by stellar evolution models including rotation-induced mixing and thermohaline instability (e.g., Lagarde et al. 2012, and the observations of Tautvaišienė et al. 2010 for $^{12}C/^{13}C$), whereas little or no difference is predicted by stellar models with the prescriptions described in Section 2.2 (see the bottom panels of Fig. 2). For this reason, our analysis in Fig. 3 focuses only on RGB stars. We discuss the differences between RGB and RC stars in Section 3.1.

In Fig. 3, the trends of $\log(N/O)$ and $\log(C/N)$ vs stellar mass as predicted by our set of stellar models qualitatively agree with the average trends that we see in the observational data for the RGB stars in our sample. Models with rotation-induced mixing and thermohaline instability predict larger depletion of $\log(C/N)$ and enhancement of $\log(N/O)$ than the models with standard mixing prescriptions. Furthermore, our reference MESA stellar evolution models predict the same $\log(C/N)$ and slightly larger $\log(N/O)$ by ≈ 0.04 dex than the models of Lagarde et al. (2012) with standard mixing prescriptions, mostly due to the slightly different $\log(N/O)$ assumed at birth in the two models. Quantitatively, all of the models in Fig. 3 predict values of $\log(N/O)$ that are too high and values of $\log(C/N)$ that are too low relative to APOGEE measurements. For $m = 1.3 M_{\odot}$, the discrepancies with the MESA models are ≈ 0.12 dex and ≈ 0.08 dex, respectively. The differences increase towards $m = 1 M_{\odot}$. These discrepancies could indicate that the models predict too much mixing, but they could also arise from incorrect assumptions about the birth abundances of C, N, and O, or from systematic errors in the APOGEE measurements.

The assumed birth abundances are based on solar ratios. Lagarde et al. 2012 adopt birth values $\log(N/O) \approx -0.86$ and $\log(C/N) \approx 0.60$, and the MESA models have $\log(N/O) \approx -0.88$. Nieva & Przybilla (2012) find $\log(N/O) \approx -0.97$ and $\log(C/N) \approx 0.54$ in a sample of B-type stars in the Solar neighbourhood. The difference from solar ratios could reflect a change with age at fixed $[Fe/H]$, or errors in the solar abundance or B-star calibrations. The differences between the assumed birth abundances and the measurements of Nieva & Przybilla (2012) are similar in magnitude to the discrepancies between the standard mixing models and the data in Fig. 3, and they have the correct sign to explain the $\log(N/O)$ discrepancy but not the $\log(C/N)$ discrepancy. The impact of changing birth abundances is not simply additive, and in Section 3.2 below we use an approximate method to assess whether a reasonable change in birth abundances can reconcile the models with the APOGEE data. The Lagarde et al. (2012) models with extra mixing predict larger $\log(N/O)$ enhancement and $\log(C/N)$ depletion, producing greater tension with the APOGEE data.

From a nucleosynthesis point of view, $\log(C/N)$ and $\log(N/O)$ are expected to have a dependence with metallicity, because of the strong metallicity-dependence of the N nucleosynthesis in AGB and massive stars (e.g., see Vincenzo et al. 2016; Vincenzo & Kobayashi 2018a,b). In particular, ^{14}N can be synthesized in the CNO cycle at the expense of the C and O nuclei present in the star at its birth. For this reason, in the late evolutionary phases of galaxies, where the chemical enrichment of AGB stars dominates N production,

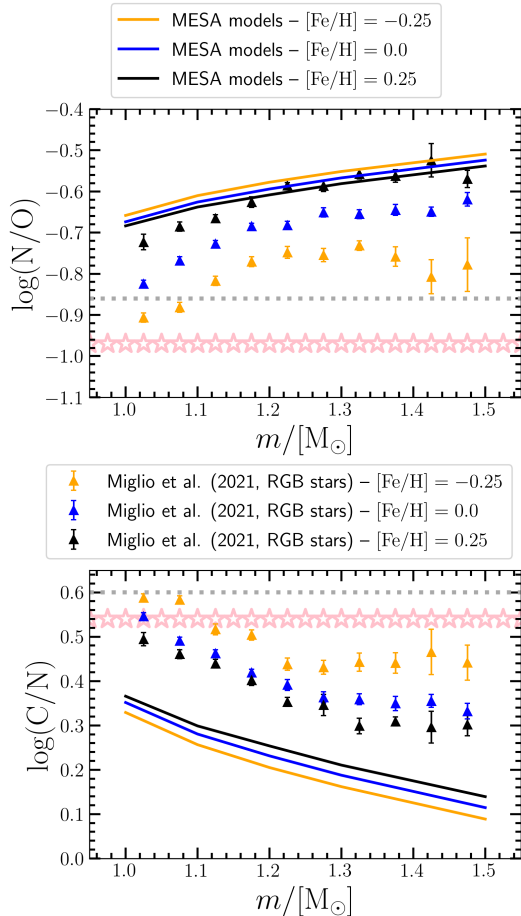


Figure 4. *Top panel:* observed average $\log(N/O)$ with corresponding uncertainty on the mean as a function of the stellar mass in the sample of stars classified as RGB by Miglio et al. (2021) (triangles with error bars), by selecting stars with $\log(g/[cm\ s^{-2}]) = 2.6 \pm 0.1$. Different colours correspond to different bins of $[Fe/H]$ with width $\Delta[Fe/H] = 0.25$, centered at the value reported in the legend. In the figure, the observations are compared with the predictions of our reference MESA stellar evolution models (solid curves with different colours). The gray horizontal line shows the assumed birth abundances in our MESA models, whereas the pink star symbols show the average abundances in a sample of B-type stars in the Solar neighbourhood as measured by Nieva & Przybilla (2012). *Bottom panel:* same as in top panel but showing our results for $\log(C/N)$ vs stellar mass. The MESA models adopt $[\alpha/Fe] = 0$ for all three values of $[Fe/H]$.

$\log(N/O)$ is predicted to steadily increase in the gas-phase, whereas $\log(C/N)$ decreases.

Metallicity has an effect on the predicted abundance variations of C, N, and O in red giants. This is illustrated in Fig. 4, which shows how $\log(N/O)$ (top panel) and $\log(C/N)$ (bottom panel) change as a function of stellar mass in our sample, when considering different $[Fe/H]$ -bins. At fixed stellar mass, stars with higher $[Fe/H]$ are observed to have larger $\log(N/O)$ and lower $\log(C/N)$. The surface abundance variations of $\log(N/O)$ and $\log(C/N)$ as predicted by our reference MESA models show an opposite trend as a function of metallicity with respect to observations, but the predicted metallicity-dependence of the atmospheric $\log(N/O)$ and $\log(C/N)$ abundance ratios in the models is much weaker than the dependence that we see in the observations. We note that the birth abundance ratios of $\log(C/N)$ and $\log(N/O)$ assumed in the models are constant as a function of $[Fe/H]$, because the models assume scaled

solar composition. Since the birth abundance ratios of $\log(N/O)$ and $\log(C/N)$ are metallicity-independent, the opposite trend of the predicted surface abundance ratio changes with increasing metallicity in Fig. 4 implies that metal-rich stars are (moderately) less affected by mixing processes than metal-poor stars.

The effects of metallicity in the models of Lagarde et al. (2012) with rotation-induced mixing and thermohaline instability are consistent with the predictions of our MESA models (Fig. 4). By assuming the stellar models of Lagarde et al. (2012), the variations due to metallicity are in the range $0.03 \lesssim |\langle \Delta \log(N/O)_{\text{mod}} \rangle| \lesssim 0.06$ and $0.05 \lesssim |\langle \Delta \log(C/N)_{\text{mod}} \rangle| \lesssim 0.12$ when moving from $Z = 0.004$ to $Z = 0.014$, and $0.04 \lesssim |\langle \Delta \log(N/O)_{\text{mod}} \rangle| \lesssim 0.1$ and $0.07 \lesssim |\langle \Delta \log(C/N)_{\text{mod}} \rangle| \lesssim 0.17$ between $Z = 0.002$ and $Z = 0.014$. From these values, the predicted dependence of $\log(C/N)$ with metallicity is almost two times larger than that of $\log(N/O)$.

The stellar models of Lagarde et al. (2012) assume that the rotation velocity does not vary as a function of metallicity, being in the range between 90 and $137\ km\ s^{-1}$ on the main sequence. Recently, Amard, Roquette, & Matt (2020) found that, at fixed stellar mass, the average rotation velocity decreases as a function of metallicity in a sample of stars in *Kepler* (see fig. 6 of Amard, Roquette, & Matt 2020), in addition to the dependence of the average rotation period with stellar mass. Charbonnel & Lagarde (2010) showed that models with higher rotation velocities at solar metallicity predict a larger depletion of $\log(C/N)$. Therefore, if we extrapolate the findings of Charbonnel & Lagarde (2010) for C/N vs v_{rot} at low metallicity, the effect of rotation would amplify the opposite dependence on metallicity which is seen between models and observations in Fig. 4. This corroborates our conclusion that the trend that we see in the observations is dominated by chemical evolution of birth abundances and not by mixing processes inside the stars.

3.1 Surface abundance distributions of red-giant branch vs red clump stars

Most of the stars in the Miglio et al. (2021) sample also have information available about their evolutionary state (for example, if they are in the RGB or RC), which was determined using the approach defined in Elsworth et al. (2019). In our analysis, we select stars in Miglio et al. (2021) with $[Fe/H]$ in the range $-0.1 \leq [Fe/H] < 0.1$ and mass in the range $0.9 \leq m < 1.6\ M_{\odot}$, and divide them in mass-bins $\Delta m = 0.1\ M_{\odot}$. Then, for each mass-bin, we compute the distribution of $\log(N/O)$ and $\log(C/N)$ of RGB and RC stars separately, using the abundance measurements from APOGEE-DR16 and the classification provided by Miglio et al. (2021). For each distribution, we compute the median values – together with the 16 and 84 percentiles – of the distributions of $\log(N/O)$ and $\log(C/N)$ for RGB and RC stars, separately.

The results of our analysis are illustrated in Fig. 5, in which the median values of $\log(N/O)$ (top panel) and $\log(C/N)$ (bottom panel) in RGB stars are compared with the corresponding values derived in RC stars. The shaded areas in the figures correspond to the 16 and 84 percentiles of the distributions around the median values. In the same figure, we also show the predictions of the stellar models of Lagarde et al. (2012) assuming $Z = Z_{\odot}$ and rotation-induced mixing plus thermohaline instability. The predictions of the models for RGB stars are shown as black dotted lines, whereas the predictions for RC stars are the red dotted lines. Similar results are found for different $[Fe/H]$ -bins, but Lagarde et al. (2012) provide stellar models over a relatively coarse grid in mass and metallicity. We do not show the predictions of our MESA stellar models, because they

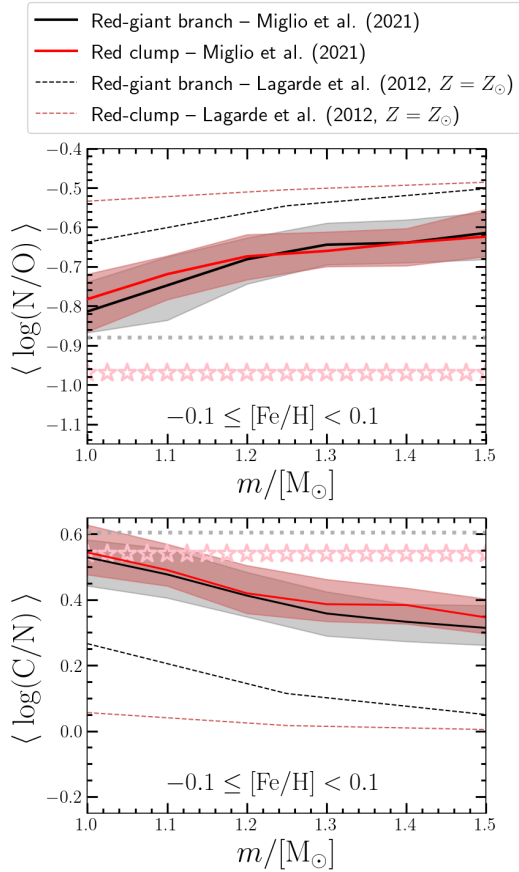


Figure 5. The observed median trends of $\log(N/O)$ (top panel) and $\log(C/N)$ (bottom panel) with corresponding 16 and 84 percentiles as a function of the stellar mass as computed from the abundance distributions of stars classified as RGB (black curves with shaded areas) and RC (red curves with shaded areas) by Miglio et al. (2021), in the range of iron abundances $-0.1 \leq [Fe/H] \leq 0.1$. The black and red dotted curves correspond to the surface abundance ratios as predicted by the stellar models of Lagarde et al. (2012) with rotation-induced mixing and thermohaline instability for RGB and RC stars, respectively, at $Z = Z_{\odot}$. The pink star symbols show the average abundances in a sample of B-type stars in the Solar neighbourhood as measured by Nieva & Przybilla (2012).

do not predict any difference in $\log(N/O)$ and $\log(C/N)$ between RGB and RC stars (see the bottom panels in Fig. 2).

The results of our analysis in Fig. 5 show that RGB and RC stars have similar $\log(N/O)$ and $\log(C/N)$ as a function of stellar mass. This is in disagreement with the predictions of the models of Lagarde et al. (2012) with extra-mixing, which predict RC stars to have systematically higher $\log(N/O)$ and lower $\log(C/N)$ than RGB stars at all stellar masses. We note that, at high stellar masses, the observed $\log(C/N)$ in RC stars are slightly larger than in RGB stars, which is the opposite of what the models of Lagarde et al. (2012) predict.

3.2 Making Model Predictions with Different Birth CNO

The stellar models predict $\log(C/H)$, $\log(N/H)$, and $\log(O/H)$, given the mass, metallicity, $[\alpha/Fe]$, and birth abundances of the stars. However, the birth abundances of young solar metallicity stars (e.g., Nieva & Przybilla 2012) may be different from the Sun’s photospheric abundances (e.g., Asplund et al. 2009). Uncertainty in the

CNO birth abundances of the order of ≈ 0.1 dex can affect the success of stellar models in reproducing the observed abundances of C, N, and O in red giants, as shown in Fig. 4.

In this Section, we provide a formalism to estimate the values of $\log(C/H)$, $\log(N/H)$, and $\log(O/H)$ that one would get with different birth abundances, by knowing the results for the solar birth abundances used in the MESA models. Our approximation is based on the assumptions that (i) the material mixed into the envelope is independent of birth abundances and (ii) the impact of birth abundances is only to change what the dredged-up material is being diluted by.

We adopt the following notation for the assumed birth abundance of the elements $Z = C, N,$ and O in the model:

$$Z_{b,0} \equiv (Z/H)_{b,0}, \quad (2)$$

in which H is dropped for notational convenience. The baseline model predictions can be expressed as follows:

$$Z_0 = Z_{b,0} + \Delta Z, \quad (3)$$

where ΔZ represents the change in the abundance of Z per unit hydrogen as predicted by MESA models because processed material is mixed into the envelope. We note that ΔZ is not in dex.

We allow a difference δZ_b in the birth abundances relative to the model assumptions. We specify these differences in dex, so that the new birth abundances are determined by the following expression:

$$Z_b = Z_{b,0} \times 10^{\delta Z_b}. \quad (4)$$

We want to know if we can reconcile the models with APOGEE data in Fig. 4, by allowing reasonable choices for δZ_b while assuming that the models correctly predict ΔZ .

The original model predictions are

$$\log(Z/H) = \log(Z_{b,0} + \Delta Z). \quad (5)$$

With a perturbation δZ_b in the birth abundances (in dex), the prediction becomes

$$\begin{aligned} Z &= Z_b \times 10^{\delta Z_b} + \Delta Z \\ &= Z_{b,0} + \Delta Z + Z_{b,0} \times (10^{\delta Z_b} - 1), \end{aligned} \quad (6)$$

in which we have used equation 4.

By putting together equations 3 and 6, we find the following equation for the change of Z after a perturbation δZ_b is applied to the assumed birth abundances:

$$\begin{aligned} \log(Z/H) - \log(Z/H)_0 &= \\ &= \log \left[\frac{Z_{b,0} + \Delta Z + Z_{b,0} \times (10^{\delta Z_b} - 1)}{Z_{b,0} + \Delta Z} \right] \\ &= \log \left[1 + 10^{-\Delta \log(Z/H)_0} (10^{\delta Z_b} - 1) \right], \end{aligned} \quad (7)$$

where

$$\begin{aligned} \Delta \log(Z/H)_0 &= \log(Z/H)_0 - \log(Z/H)_{b,0} \\ &= \log \left[1 + \frac{\Delta Z}{Z_{b,0}} \right]. \end{aligned} \quad (8)$$

Qualitatively, equation 7 explains why, in Fig. 4, the discrepancy is larger for small masses than for large masses. Because $\Delta \log(N/H)_0$ increases with mass in Fig. 2, the correction expressed by equation 7 is bigger when the mass is smaller.

In our analysis, we assume that N birth abundances scale with metallicity according to the following relation:

$$\delta N_b = \delta N_{\odot} + 0.7 \times [Fe/H], \quad (9)$$

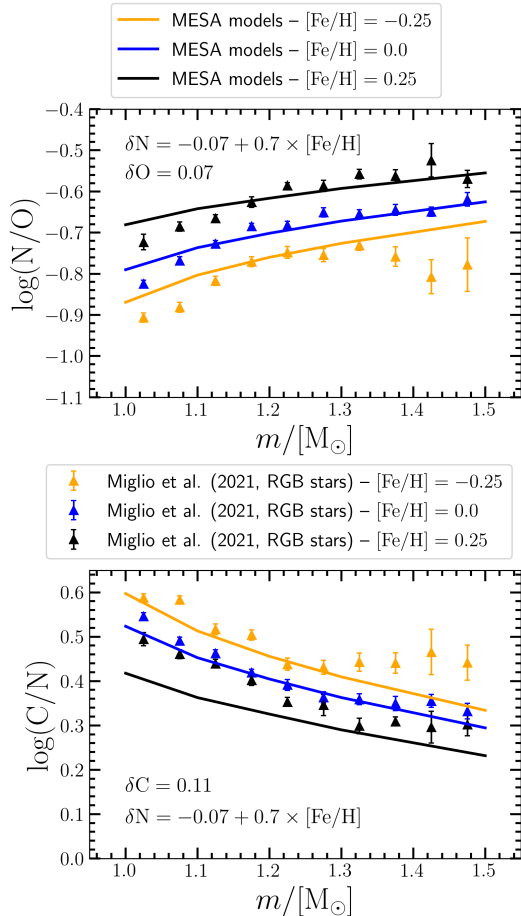


Figure 6. Similar to Fig. 4 but showing the effect of perturbing the assumed birth abundances at $Z = Z_{\odot}$ in our MESA models according to the formalism outlined in Section 3.2, in order to reconcile the observed relations of $\log(N/O)$ vs mass (top panel) and $\log(C/N)$ vs mass (bottom panel) with the models predictions.

where δN_{\odot} corresponds to the perturbation on the N birth abundance at $Z = Z_{\odot}$ assumed by our MESA models taken from Asplund et al. (2009), and the slope of 0.7 is based on our findings in Fig. 11 (see also Section 5 for a detailed discussion), which shows abundance measurements of $\log(N/O)$ in the ISM of galaxies and the calibration relation for the gas-phase $\log(N/O)$ vs $\log(O/H) + 12$ proposed by Dopita et al. (2016).

For C and O, we assume that the birth abundances do not vary with metallicity:

$$\begin{aligned} \delta C_b &= \delta C_{\odot}, \\ \delta O_b &= \delta O_{\odot}. \end{aligned} \quad (10)$$

In Fig. 6, we show that MESA predictions can be reconciled with the observed $\log(N/O)$ vs mass and $\log(C/N)$ vs mass in different metallicity ranges by assuming $\delta C_{\odot} = 0.11$, $\delta N_{\odot} = -0.07$, and $\delta O_{\odot} = 0.07$. These values of δN_{\odot} and δO_{\odot} relative to Asplund et al. (2009) are similar to the differences between the abundances of Nieva & Przybilla (2012) (who measured $\log(C/H) = 8.33$, $\log(N/H) = 7.79$, $\log(O/H) = 8.76$ in nearby B-type stars) and those of Asplund et al. (2009) (who measured $\log(C/H) = 8.43$, $\log(N/H) = 7.83$, $\log(O/H) = 8.69$ in the Sun photosphere). However, they differ for δC_{\odot} by 0.2 dex, since the difference between

Nieva & Przybilla (2012) and Asplund et al. (2009) is -0.1 dex for C.

Fig. 6 shows agreement with the APOGEE $\log(N/O)$ and $\log(C/N)$ at the ≈ 0.05 dex level for most masses and metallicities, with differences rising to ≈ 0.1 dex in some bins. This agreement shows that the larger differences seen in Figs. 3 and 4 are plausibly explained by incorrect assumptions about birth abundances rather than incorrect mixing predictions, perhaps in combination with zero-point calibration offsets in the abundance measurements themselves. However, it does not guarantee that the mixing predictions are accurate. The success of this assumption in explaining the observed metallicity dependence of $\log(N/O)$ and $\log(C/N)$ supports our conjecture that chemical evolution of N birth abundances dominates these trends.

4 CORRECTING APOGEE ABUNDANCES FOR EVOLUTIONARY EFFECTS

The predictions of our reference MESA stellar evolution models are used to compute the surface abundance changes $\Delta \log(C/H)$, $\Delta \log(N/H)$, and $\Delta \log(O/H)$ in the stars of our sample, depending on their surface gravity, mass, $[Fe/H]$ abundance, and $[\alpha/Fe]$ ratio. We do not interpolate or extrapolate in the grid of stellar evolution tracks, but use the closest point to compute a theoretical correction due to mixing for each star in the sample. The $[\alpha/Fe]$ ratio of the stars is taken from the quantity ALPHA_M in the APOGEE-DR16 catalogue.

If our abundance and mass measurements and our mixing models were perfectly accurate, it would be preferable to correct ΔN , ΔC , and ΔO as described in Section 3.2. However, if the mixing corrections is comparable to the observed surface abundance, then the implied change in $\log(C/H)$, $\log(N/H)$, and $\log(O/H)$ can become very large, and the implied birth abundance can even become negative. We have therefore chosen to apply the $\Delta \log(C/H)$, $\Delta \log(N/H)$, and $\Delta \log(O/H)$ predicted by the models, which we find yields similar results on average and is more robust to imperfections in the data and models.

4.1 The variation of $\log(N/O)$

The results of our analysis for $\log(N/O)$ are illustrated in Fig. 7, which compares $\log(N/O)$ vs age (panel a1) and $\log(N/O)$ vs $[Fe/H]$ (panel a2) as observed in the stars of our sample with the trends corrected for mixing effects following our reference MESA stellar evolution models (panels b1 and b2).

Without a correction, a strong correlation is observed between $\log(N/O)$ and age at fixed $[Fe/H]$ abundance (see panels a1 and a2). When we apply the abundance corrections due to mixing as predicted by our reference MESA stellar models, the age-dependence of $\log(N/O)$ is effectively removed for ages $\lesssim 10$ Gyr (see panels b1 and b2). At older ages, there is a population of metal-poor red giants with corrected $\log(N/O) \approx -1.5$, consistent with the observations in metal-poor halo stars (e.g., Spite et al. 2005), damped-Ly α systems (e.g. Pettini et al. 2002, 2008), and metal-poor star-forming blue compact dwarf galaxies (e.g., Berg et al. 2012; Izotov, Thuan, & Guseva 2012; James et al. 2015). The plateau in $\log(N/O)$ at low metallicity has been used to infer the presence of a primary N component from massive stars (see Matteucci 1986; Chiappini, Romano, & Matteucci 2003; Chiappini, Matteucci, & Ballero 2005; Vincenzo et al. 2016).

After correcting the observed $\log(N/O)$ for the mixing, we

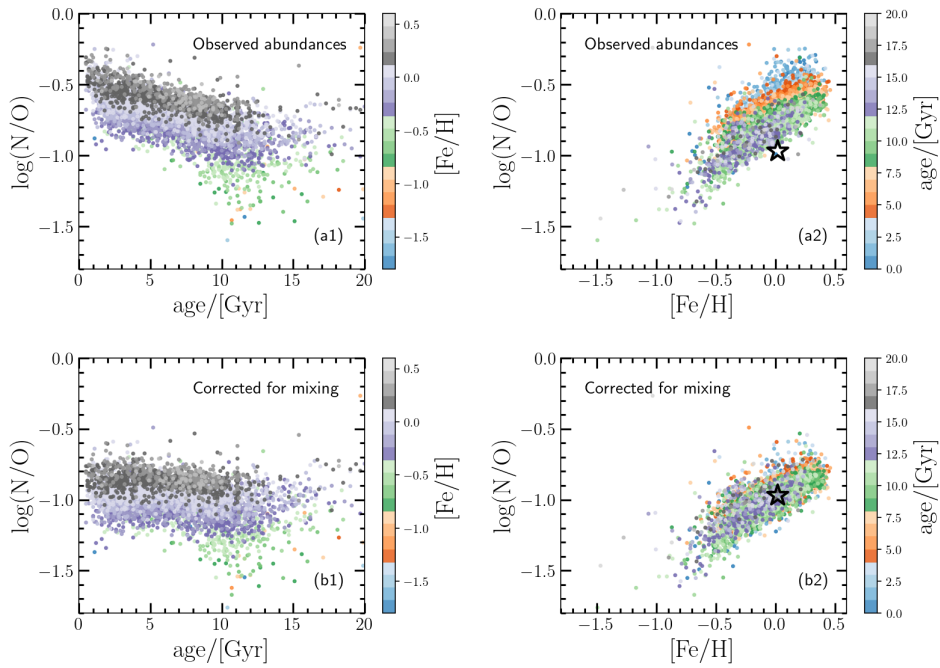


Figure 7. Panel (a1): observed $\log(N/O)$ vs age, by using the ages from the analysis of Miglio et al. (2021) and the abundances from APOGEE-DR16; the color-coding corresponds to the $[Fe/H]$ abundance of the stars. Panel (a2): observed $\log(N/O)$ vs $[Fe/H]$, with the color-coding representing the ages of the stars from the analysis of Miglio et al. (2021). The black star shows the observed average abundances in a sample of B-type stars in the Solar neighbourhood by Nieva & Przybilla (2012). Panel (b1): predicted $\log(N/O)$ vs age when the surface abundances of C and N are corrected for mixing effects using the predictions of our reference MESA stellar evolution models. Panel (b2): predicted $\log(N/O)$ vs $[Fe/H]$ when the surface abundances of C and N are corrected for mixing effects as in panel (b1). The black star shows the results of the abundance analysis of Nieva & Przybilla (2012) for a homogeneous sample of B-type stars in the Solar neighbourhood.

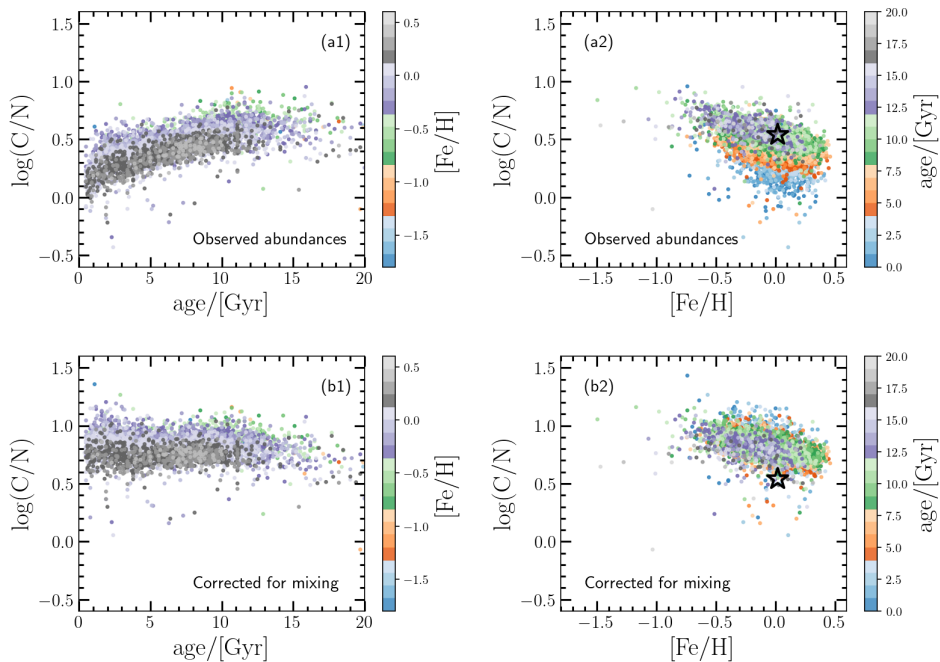


Figure 8. Similar set of panels as in Fig. 7 but showing the results of our analysis for the $\log(C/N)$ vs age and $[Fe/H]$ relations in the sample of Miglio et al. (2021). The black star in (a2) and (b2) shows the observed average abundances in a sample of B-type stars in the Solar neighbourhood by Nieva & Przybilla (2012).

are left with a strong dependence of $\log(N/O)$ on $[Fe/H]$. This is in agreement with observations in nearby spiral galaxies, which show striking relations between $\log(N/O)$ and $\log(O/H) + 12$ (e.g. Henry, Edmunds, & Köppen 2000; Pettini et al. 2002, 2008; Pilyugin, Vílchez, & Thuan 2010; Belfiore et al. 2017; Berg et al. 2020), and stellar abundance measurements in our Galaxy (e.g., Magrini et al. 2018 with Gaia-ESO survey). As discussed by Vincenzo & Kobayashi (2018b), the $\log(N/O)$ vs. metallicity diagram is regulated – to first order – by the nucleosynthesis of N, which strongly depends on metallicity, being mainly synthesized in the CNO cycle at the expense of the C and O nuclei already present in the stars at birth. Secondary effects regulating the evolution of stellar and gas-phase abundances in $\log(N/O)$ vs $\log(O/H) + 12$ can be variations in the star formation efficiency and bursts of star formation caused by sudden inflows of gas, because of the different time scales with which N and O are released by dying stellar populations in galaxies (see Vincenzo et al. 2016).

In Fig. 7, we show that our predictions for the corrected $\log(N/O)$ vs $[Fe/H]$ are consistent with the average measurements of Nieva & Przybilla (2012) in a sample of B-type stars in the Solar neighbourhood, providing indication that our reference MESA models are able to effectively capture the main mixing evolutionary processes affecting N abundances in stars.

4.2 The variation of $\log(C/N)$

The results of our analysis for $\log(C/N)$ are shown in Fig. 8. Similarly to $\log(N/O)$, there is a strong dependence of observed $\log(C/N)$ as a function of age in our sample; moreover, at fixed age, stars with increasing metallicities are observed to have higher $\log(C/N)$. The strong correlation between $\log(C/N)$ and age/mass in red giants is known to be due to internal mixing processes, which are more important in stars with larger masses, explaining why $\log(C/N)$ is used as an age diagnostic for red giants (e.g., Iben 1964; Salaris et al. 2015; Masseron & Gilmore 2015; Martig et al. 2016; Miglio et al. 2021). When we correct the observed $\log(C/N)$ to account for the mixing processes, we effectively remove the strong age-dependence of $\log(C/N)$, and only the metallicity dependence is left (see panels b1-b2), such that stars with higher metallicities have – on average – lower $\log(C/N)$. This is expected from a nucleosynthesis point of view because of the opposite metallicity-dependence of the C and N yields from AGB and massive stars (e.g., Vincenzo & Kobayashi 2018a). Models with diffusive convective core overshooting efficiency $f_{ov,core} = 0.02$ predict that stars with mass $m \geq 2 M_{\odot}$ have their N abundances after the first dredge-up enhanced by ≈ 0.04 dex with respect to our reference models assuming $f_{ov,core} = 0$; this could help flattening the small bump in the corrected C/N ratios at ages about ≈ 1 Gyr and $[Fe/H] \approx 0$.

The mixing-corrected $\log(C/N)$ ratios as predicted by our reference MESA models lie above the average measurements of Nieva & Przybilla (2012) at $[Fe/H] \approx 0$ in a sample of B-type stars in the Solar neighbourhood. Since the main effect of the mixing processes is enhancing the atmospheric N abundances (see Fig. 2) at the expense of C and O, it is difficult to reconcile the fact that our models are able to reproduce the enhancement of $\log(N/O)$ but overestimate the depletion of $\log(C/N)$. Systematic uncertainties of the order of ≈ 0.05 dex in the C and N abundance measurements of APOGEE-DR16, such that C would be increased and N decreased, would help reduce the discrepancy that we find between the mixing-corrected $\log(C/N)$ as predicted by our MESA models and the average measurement of Nieva & Przybilla (2012).

4.3 C, N, O surface abundance variations in high- α and low- α stars

We divide the red giant stars in the sample of Miglio et al. (2021) between high- α and low- α by adopting the following demarcation line, which approximately separates them in the $[Mg/Fe]$ vs $[Fe/H]$ diagram:

$$[Mg/Fe] = 0.125 - 0.11 \times [Fe/H]. \quad (11)$$

For each star in the sample we apply the same analysis as discussed in the previous subsections. We aim at quantifying the surface abundance variations in the high- α thick-disc stars with respect to those in the low- α thin-disc. In Fig. 9, we show the results of our analysis for $[C/Mg]$ (first column), $[N/Mg]$ (second column), and $[N/O]$ (third column). In particular, the upper panels show how $[C/Mg]$ vs $[Mg/H]$, $[N/Mg]$ vs $[Mg/H]$, and $[N/O]$ vs $[O/H]$ are observed to differ between the thick-disc (red points) and thin-disc (blue points) stars of our sample. After we apply the surface abundance corrections predicted by our reference MESA stellar evolution models, we obtain surface abundances of $[C/Mg]$ vs $[Mg/H]$, $[N/Mg]$ vs $[Mg/H]$, and $[N/O]$ vs $[O/H]$ shown in the middle panels of Fig. 9. Finally, the bottom panels show the model predicted variations of $\log(C/H)$, $\log(N/H)$, and $\log(O/H)$ for thick- and thin-disc stars as a function of $[Fe/H]$.

The largest abundance corrections are predicted for thin-disc stars. In particular, the N abundances of thin-disc stars are predicted to be enhanced by as much as ≈ 0.45 dex with respect to the birth abundances. C abundances are predicted to be moderately depleted, with an upper limit in their depletion of the order of ≈ 0.23 dex. We note that the observed $[O/Fe]$ vs $[Fe/H]$ diagram and its bimodal distribution between thick- and thin-disc stars (e.g., see the recent Vincenzo et al. 2021) are not affected much by mixing processes; the predicted corrections for O are in the range $-0.01 \leq \Delta \log(O/H) < 0.02$, comparable to observational uncertainties.

After correction, both $[C/Mg]$ and $[N/Mg]$ trends still show a substantial separation between the high- α and low- α populations, indicating that both elements have significant contributions from a “delayed” source, most likely AGB enrichment, in addition to prompt enrichment by core-collapse SNe. For $[C/Mg]$, the sequence separation is comparable to that found in GALAH-DR2 by Griffith, Johnson, & Weinberg (2019), but the metallicity dependence is opposite, rising rather than falling with $[Mg/H]$. For $[N/Mg]$, the strongly rising metallicity dependence for both populations is a sign of metallicity-dependence N yields. In APOGEE data, $[O/Mg]$ ratios are near solar over $-0.7 \lesssim [Mg/H] \lesssim 0.5$ for both high- α and low- α populations (Weinberg et al. 2019), consistent with both elements being produced by core-collapse SNe with IMF-averaged yields that are metallicity independent. Not surprisingly, we find that the trends of $[N/O]$ vs $[O/H]$ are nearly identical to the trends of $[N/O]$ vs $[Mg/H]$.

The idea of using C/N ratios as a stellar age diagnostic in APOGEE data (Masseron & Gilmore 2015; Martig et al. 2016) is based on the expectation that the surface abundances in APOGEE red giants are driven largely by internal mixing and thus depend strongly on stellar mass. Calibration against asteroseismic masses/ages supports this approach (Pinsonneault et al. 2018; Miglio et al. 2021), as above in Fig. 8(a). However, Figs. 8(b) and 9 show that there are also significant dependencies of both C and N abundances on $[Fe/H]$ and on $[\alpha/Fe]$. These birth abundance trends should be taken into account when using C/N ratios or spectroscopic diagnostics sensitive to them to estimate red giant ages.

Figure 10 places the measurements of our asteroseismic sample

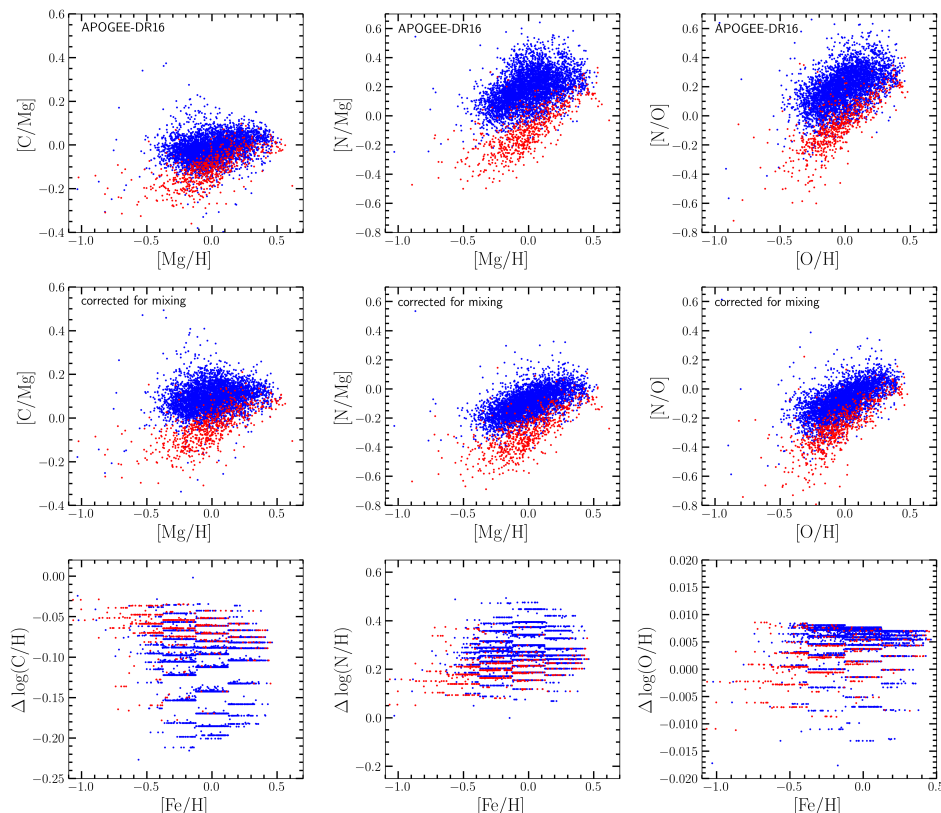


Figure 9. *Top panels:* the observed $[C/Mg]$ vs $[Mg/H]$ (first column), $[N/Mg]$ vs $[Mg/H]$ (second column), and $[N/O]$ vs $[O/H]$ (third column) as observed in APOGEE-DR16, by using the sample of stars of Miglio et al. (2021); to quantify the impact of evolutionary mixing effects in the two sequences, stars in the high- α component are shown in red, whereas stars in the low- α component are shown in blue, by using equation 11 reported in the main text. *Middle panels:* same as in the top panels, but the evolutionary effects due to mixing are taken into account by using our reference MESA stellar evolution models. Note the different vertical axis ranges for the left panels, representing the small dynamic range of $[C/Mg]$. *Bottom panels:* $\Delta \log(C/H)$, $\Delta \log(N/H)$, and $\Delta \log(O/H)$ as predicted for the stars when passing from the top to the bottom panel, by accounting for the evolutionary effects on the surface abundances due to mixing processes.

in the broader context of APOGEE-DR16 disk CNO measurements. We plot surface abundances $[C/N]$, $[N/O]$, and $[Mg/Fe]$ against spectroscopic $\log(g)$ over the range $1 \leq \log(g/[cm\ s^{-2}]) \leq 3.5$ for stars in the high- α (red) and low- α (blue) populations and for the Miglio et al. (2021) stars (larger black dots). Consistent with the findings of Shetrone et al. (2019) based on APOGEE-DR13 (Holtzman et al. 2018; Jönsson et al. 2018), the $[C/N]$ and $[N/O]$ ratios of lower metallicity stars ($[Fe/H] \lesssim -0.5$) show moderate trends with $\log(g)$ for stars more luminous than the RC (i.e., $\log(g) < 2.5$). The asteroseismic sample contains too few low metallicity stars to reveal these trends. Shetrone et al. (2019) interpret the decline in $[C/N]$, which becomes much more prominent at still lower metallicities, as a sign of extra mixing above the bump in the RGB luminosity function. For comparison, in the top row we show the predictions of the Lagarde et al. (2012) models with rotation and thermohaline instability. At $Z = 0.004$ ($[Fe/H] \approx -0.6$), these models predict a much stronger $\log(g)$ trend than seen in the APOGEE observations. Together with the similarity of RC and RGB ratios (Figure 5), this comparison further indicates that extra mixing in the Lagarde et al. (2012) models is too strong, perhaps because of the numerical or physical treatment of thermohaline instability (see, e.g., Constantino et al. 2015, 2016; Constantino, Campbell, & Lattanzio 2017).

At low metallicities, the high- α and low- α populations show clear differences in $[C/N]$ and $[N/O]$ at all $\log(g)$. The two populations converge at high metallicity as the separation in $[\alpha/Fe]$

itself becomes smaller. Figure 9 showed similar behavior for the asteroseismic sample in $[C/Mg]$, $[N/Mg]$, and $[N/O]$, and while correction for mixing shifts both the high- α and low- α populations in these diagrams, it does not remove the separation between them. We conclude that this separation is, unsurprisingly, a consequence of different birth abundances. To interpret this difference, it is useful to recall that the “low- α ” stars are really Fe rich — for a given level of core collapse supernova elements such as O and Mg they have a larger contribution of Fe from Type Ia supernovae. The higher $[N/O]$ in this population implies that N enrichment at least partly tracks this extra Fe enrichment, probably because it also comes from a time-delayed source (AGB stars rather than Type Ia supernovae). The lower $[C/N]$ in this population implies that C enrichment is not tracking Type Ia Fe to the same degree. C behaves partly but not entirely like an α element — in Figure 9 it shows a separation between low- α and high- α populations, but only by ~ 0.1 dex or less. This implies a large core collapse supernova contribution to C, in agreement with theoretical models (e.g., Andrews et al. 2017; Rybizki, Just, & Rix 2017; Griffith et al. 2021).

Figure 9 and 10 suggest some caution in using C/N ratios or spectroscopic diagnostics that trace these ratios as age indicators for red giants. For stars that are matched in $[Fe/H]$ and $[\alpha/Fe]$, the differences in surface C/N ratios should mainly reflect differences in the degree of internal mixing, which in turn depend on mass and thus (for evolved stars) on age. However, for stars with different $[Fe/H]$ or

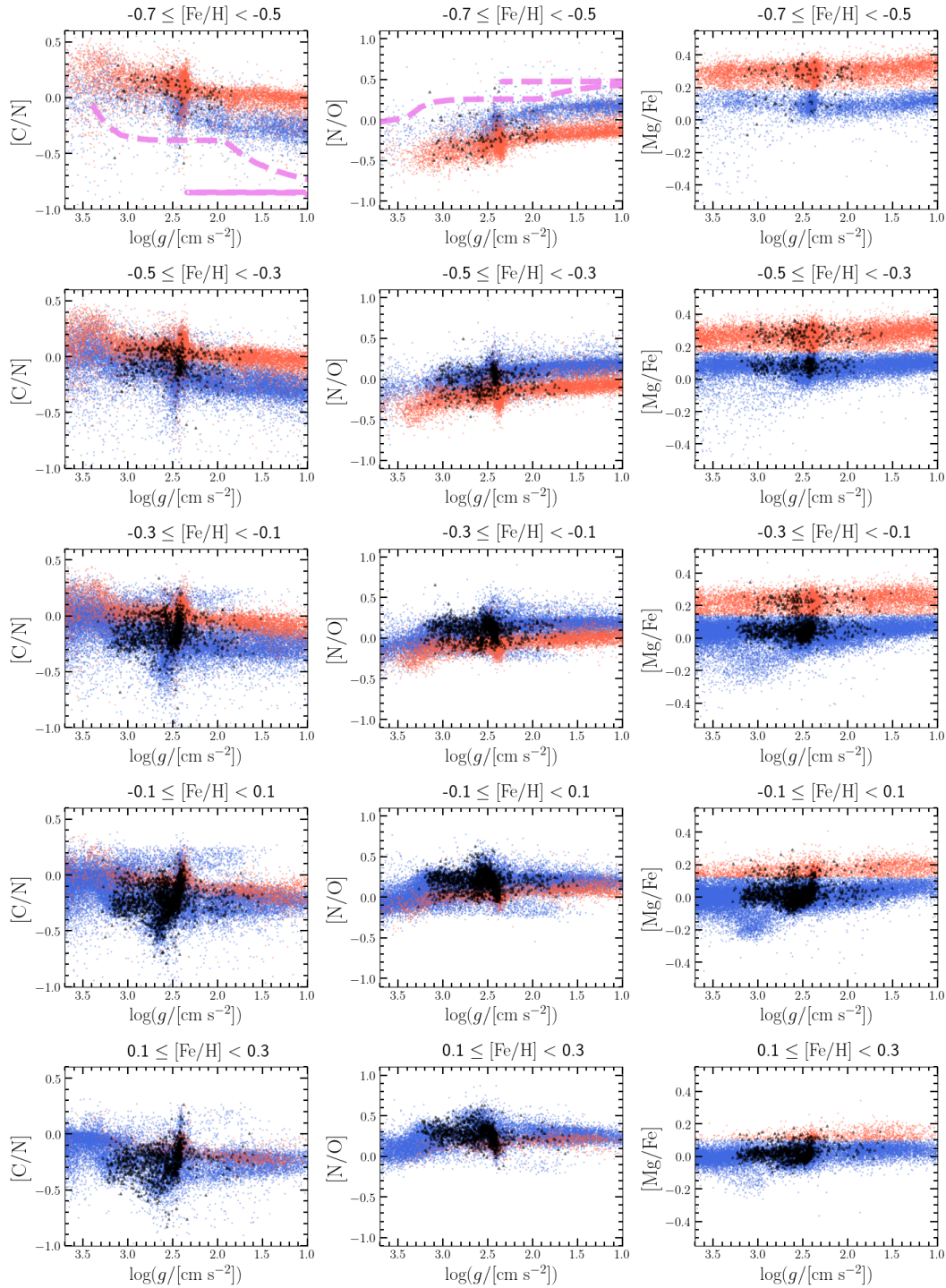


Figure 10. The observed [C/N] (first column), [N/O] (second column), and [Mg/Fe] (third column) as a function of $\log(g)$ in the high- α sequence (red points) and low- α sequence (blue points) from APOGEE-DR16, by assuming $\text{SNR} > 80$. Different rows correspond to different ranges of [Fe/H] abundances. The black triangles correspond to our sample of red giants from Miglio et al. (2021). The magenta dashed lines in the top row show the predictions of the models of Lagarde et al. (2012) for a star with initial mass $m = 1 M_{\odot}$ and metallicity $Z = 0.004$ assuming rotation-induced mixing and thermohaline instability.

different $[\alpha/\text{Fe}]$ at the same [Fe/H], differences in surface C/N may also be affected by differences in birth abundances at the 0.1-0.2 dex level. One way forward is to use mixing-corrected samples with asteroseismic masses to define empirical trends of birth abundances (e.g., the middle row of Figure 9), then use the *differences* from these

expected birth abundances, $\Delta[\text{C/N}]$ and $\Delta[\text{N/O}]$, as the diagnostic for ages in stars that do not have asteroseismic masses.

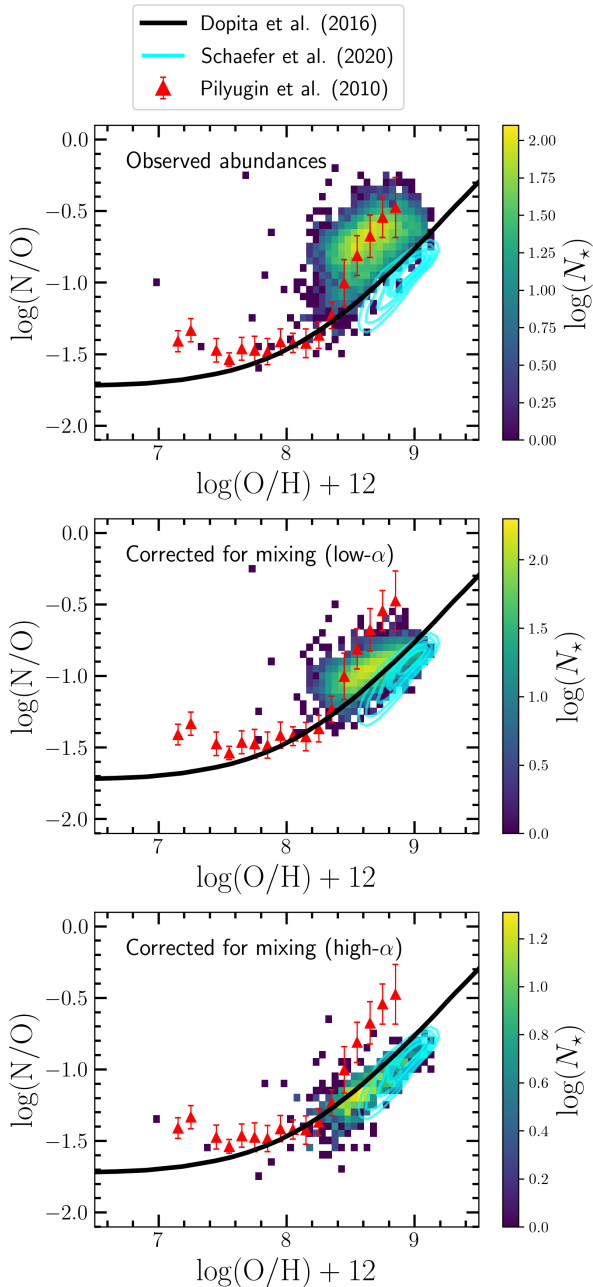


Figure 11. Comparison between $\log(N/O)$ vs $\log(O/H) + 12$ as observed in the sample of Miglio et al. (2021, 2-D histograms in both panels) and observations in resolved HII regions of nearby galaxies (Pilyugin, Vílchez, & Thuan 2010, “ONS” calibration) and unresolved star-forming regions of external galaxies Schaefer et al. (2020, “R23” calibration of Maiolino et al. 2008). The black solid line corresponds to the metallicity calibration relation as proposed by Dopita et al. (2016). The 2-D histogram in the top panel shows the observed APOGEE-DR16 abundances of the red giants in Miglio et al. (2021). The 2-D histograms in the middle and bottom panels show the results of our analysis for stars in the low- and high-[Mg/Fe] sequences, respectively (see equation 11), when we correct the observed abundances of O and N for mixing processes.

5 COMPARISON WITH GAS-PHASE ABUNDANCES

Oxygen abundance measurements in HII regions from strong nebular lines are affected by large systematic uncertainty. Such measurements usually rely on indexes and calibration relations based on sub-samples where weak auroral lines are available for the so-called direct or T_e -method to be applied. Uncertainties in the derived O abundances can be as large as ≈ 0.6 dex (e.g., Kewley & Ellison 2008; Moustakas et al. 2010; López-Sánchez et al. 2012; Blanc et al. 2015; Belfiore et al. 2017), and widely used calibrations rely on indexes based on $\log(N/O)$ (see the discussion and references in Schaefer et al. 2020).

Since the average $\log(N/O)$ vs $\log(O/H) + 12$ relation is mostly determined by the nucleosynthesis of N, which strongly depends on metallicity, the surface N and O abundances in red giants corrected for the mixing processes can be used to constrain the best calibration relation to measure $\log(O/H) + 12$ and $\log(N/O)$ in the HII regions of our Galaxy and external galaxies in the high-metallicity regime where weak auroral lines are not available.

The results of our analysis are shown in Fig. 11. In the bottom panel, we compare $\log(N/O)$ vs $\log(O/H) + 12$ as observed in the red giants of Miglio et al. (2021, 2-D histogram) with the N and O abundance measurements in a sample of resolved HII regions in extragalactic systems (Pilyugin, Vílchez, & Thuan 2010, “ONS” calibration); we also show the abundance measurements in the star-forming regions of large samples of galaxies with different stellar mass by Schaefer et al. (2020, “R23” calibration of Maiolino et al. 2008), and the calibration relation proposed by Dopita et al. (2016), which was also used as an observational constraint by Vincenzo & Kobayashi (2018a,b) for a comparison with the predictions of their cosmological simulation for N and O abundances in galaxies.

If our reference MESA stellar evolution models are able to correctly characterize the surface abundance variations of N and O in red giants of different mass and metallicity, then the best agreement with the predicted surface abundance measurements corrected for mixing is obtained with the calibration relation proposed by Dopita et al. (2016). Interestingly, when we apply the surface abundance correction, we can obtain a better agreement also with the observations of Schaefer et al. (2020) for MaNGA galaxies, who assumed the “R23” calibration of Maiolino et al. (2008), whereas the “ONS” calibration of Pilyugin, Vílchez, & Thuan (2010) seems to be disfavoured. A similar conclusion was found in the analysis of Magrini et al. (2018), who presented MW stellar abundances of N and O as measured by the Gaia-ESO spectroscopic survey. In detail, our results for low- α stars lie slightly above the Dopita et al. (2016) calibration (by about 0.1 dex), while our results for high- α stars is slightly below the Dopita et al. (2016) calibration (by about 0.05 dex) and agree well with the MaNGA results.

In Fig. 12, we compare the evolution-corrected $\log(N/O)$ vs $\log(O/H) + 12$ (top panel) and $\log(C/N)$ vs $\log(O/H) + 12$ (bottom panel) in our sample of red giants with the predicted stellar abundances in a simulated star-forming disc galaxy selected in the cosmological hydrodynamical simulation of Vincenzo & Kobayashi (2018a,b), corresponding to Galaxy B in Vincenzo et al. (2019). The agreement is excellent for $\log(N/O)$ vs $\log(O/H) + 12$, but there is a strong tension for $\log(C/N)$ between cosmological simulations and the results our analysis based on the MESA models. The simplest interpretation of this discrepancy is that the C yields adopted in these simulations are too high.

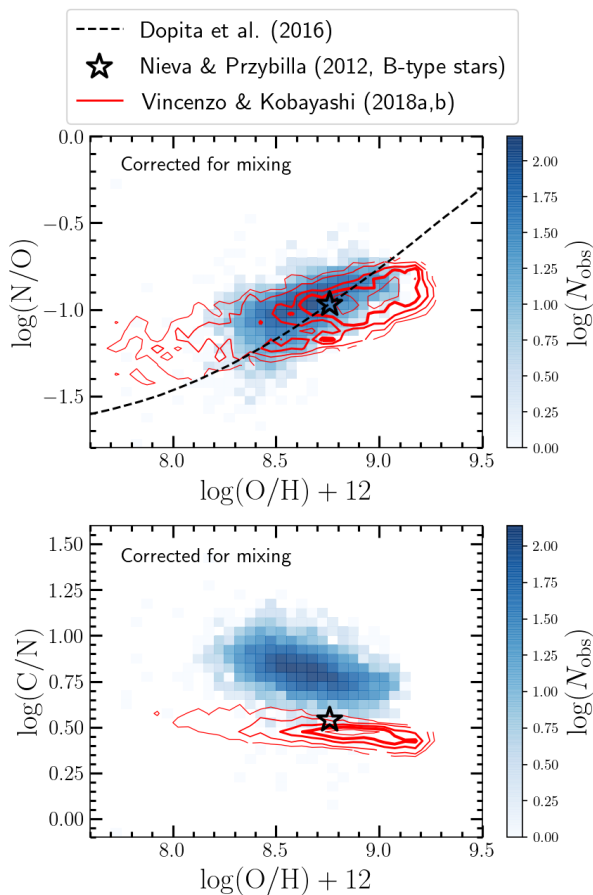


Figure 12. Comparison between the evolution-corrected $\log(N/O)$ vs $\log(O/H) + 12$ (top panel) and $\log(C/N)$ vs $\log(O/H) + 12$ (bottom panel) in the sample of Miglio et al. (2021), 2-D histograms in both panels) with the predicted stellar abundances in Galaxy B of Vincenzo et al. (2019, red solid contours corresponding to the normalized number densities of 10, 20, 40, 60, and 80 per cent) from the cosmological hydrodynamical simulation of Vincenzo & Kobayashi (2018a,b). The black dashed line corresponds to the metallicity calibration relation as proposed by Dopita et al. (2016). The black star symbols show the average abundances in a sample of B-type stars in the Solar neighbourhood as measured by Nieva & Przybilla (2012).

6 CONCLUSIONS

In this paper, we have studied how $\log(C/N)$ and $\log(N/O)$ evolve in a sample of red giants as functions of their mass, metallicity, and evolutionary phase, by using chemical abundance measurements from the APOGEE collaboration (Majewski et al. 2017; DR16 public release of Ahumada et al. 2020) and precise masses and radii from the asteroseismic analysis of Miglio et al. (2021), which was performed on the light curves of the stars as observed the *Kepler* mission (Borucki et al. 2010; see Section 2.1 for more details).

Observational data have been compared with the predictions of our reference set of stellar evolution models developed with the code MESA (Paxton et al. 2011, 2013, 2015, 2018) by assuming standard mixing prescriptions for a fine grid of stellar masses and $[Fe/H]$ abundances, with $[\alpha/Fe] = 0.0, 0.2,$ and 0.4 (see Section 2.2 for more details). We have also analysed an alternative set of stellar evolution models developed by Lagarde et al. (2012) with the code STAREVOL (Siess, Dufour, & Forestini 2000; Palacios et al. 2003, 2006; Decressin et al. 2009a) for a relatively coarse grid of masses and metallicities, by assuming either standard mixing

prescriptions or extra-mixing mechanisms (rotation-induced mixing and thermohaline instability; see Section 2.3 for more details).

Our conclusions can be summarized as follows.

(i) By selecting the stars classified as RGB in the analysis of Miglio et al. (2021), the observed $\log(N/O)$ ratios are increasingly enhanced at the stellar surface when moving to larger masses at fixed metallicity and surface gravity. Conversely, the observed $\log(C/N)$ ratios are increasingly depleted at the surface. Our reference models with standard mixing prescriptions can qualitatively reproduce these trends. As expected, models with extra-mixing predict larger $|\Delta \log(N/O)|$ and $|\Delta \log(C/N)|$ at fixed stellar masses than models with standard mixing prescriptions, but the predicted behaviour of $\log(N/O)$ and $\log(C/N)$ vs stellar mass is similar in both cases. Over the surface gravity range probed by our sample, $1.5 \lesssim \log(g/[cm\ s^{-2}]) \lesssim 3.3$, the trends of observed abundances are nearly flat in $\log(g)$ at fixed stellar mass, in agreement with the predictions of the models.

(ii) The slope of $\log(N/O)$ and $\log(C/N)$ as a function of stellar mass is observed to change at $m \approx 1.2 M_{\odot}$, which approximately divides stars with a radiative core in the MS from stars with a convective core.

(iii) The stellar models of Lagarde et al. (2012) with rotation-induced mixing and thermohaline instability predict RC stars to have higher $\log(N/O)$ and lower $\log(C/N)$ ratios than RGB stars of the same mass and metallicity. In the observed sample, RGB and RC stars are characterized by similar median values of $\log(N/O)$ and $\log(C/N)$ as a function of stellar mass. If we also look at the tails of the observed distributions, then the disagreement between the extra-mixing model predictions and observations is particularly evident for $\log(C/N)$.

(iv) We develop a formalism to calculate $\log(C/H)$, $\log(N/H)$, and $\log(O/H)$ that one would get with different birth abundances from those used in the MESA models. Differences of the order of $\delta C_{\odot} = 0.11$, $\delta N_{\odot} = -0.07$, and $\delta O_{\odot} = 0.07$ relative to Asplund et al. (2009), together with a metallicity trend $\delta(N) \propto 0.7 \times [Fe/H]$, can reproduce the observed behaviour of $\log(N/O)$ and $\log(C/N)$ vs mass in different metallicity ranges for our MESA standard mixing models (see Fig. 6). The quantities δN_{\odot} and δO_{\odot} are consistent with the difference between Nieva & Przybilla (2012) for a sample of B-type stars in the Solar neighbourhood and Asplund et al. (2009) for the solar photosphere; conversely, δC_{\odot} differs by 0.2 dex with respect to the difference between Nieva & Przybilla (2012) and Asplund et al. (2009) (which is -0.1 dex). The assumed metallicity trend for the birth abundances of N is based on widely used metallicity calibrations to measure gas-phase abundances from strong nebular emission lines (see Fig. 11).

(v) When moving to younger ages, red giants are observed to have increasingly high $\log(N/O)$ and low $\log(C/N)$ ratios at fixed $[Fe/H]$ abundance. If we fix the stellar age, $\log(N/O)$ and $\log(C/N)$ correlate with $[Fe/H]$, such that more metal-rich stars have higher $\log(N/O)$ and lower $\log(C/N)$ ratios. When we apply the abundance corrections due to mixing as predicted by our reference stellar evolution models, the observed age-dependence of $\log(N/O)$ and $\log(C/N)$ is effectively removed. Since the predicted abundance corrections weakly depend on metallicity, after we correct the observed abundances for the mixing evolutionary processes, we are left with a residual dependence of $\log(N/O)$ and $\log(C/N)$ on $[Fe/H]$, which is particularly strong for $\log(N/O)$, as expected by the nucleosynthesis studies of C and N in galaxies (e.g., see Vincenzo et al. 2016; Vincenzo & Kobayashi 2018a, and references therein).

(vi) The largest abundance corrections are predicted for thin-

disc stars, i.e., stars with approximately solar $[\alpha/\text{Fe}]$ ratios. The $[\text{N}/\text{H}]$ ratios of thin-disc stars are predicted to be enhanced by up to 0.45 dex with respect to the birth abundances. $[\text{C}/\text{H}]$ ratios are predicted to be moderately depleted by up to 0.23 dex. The observed $[\text{O}/\text{Fe}]$ vs $[\text{Fe}/\text{H}]$ diagram and its bimodal distribution between thick- and thin-disc stars is not affected by mixing processes; the predicted corrections for O are in the range $-0.01 \leq \Delta \log(\text{O}/\text{H}) < 0.02$.

(vii) Thick-disc (high $[\alpha/\text{Fe}]$) stars are observed to have systematically higher $[\text{C}/\text{N}]$ and lower $[\text{N}/\text{O}]$ than thin-disc stars with the same metallicity and surface gravity. The difference persists after mixing corrections, so it is likely due to different C, N, and O birth abundances between thick- and thin-disc stars. This difference can have a significant impact on spectroscopic age determinations based on C/N if ignored. The trend of $[\text{C}/\text{N}]$ with $[\text{Fe}/\text{H}]$ could also affect C/N-based age determinations.

(viii) Our asteroseismic sample does not have enough low metallicity stars to reveal the dependence of observed $[\text{C}/\text{N}]$ and $[\text{N}/\text{O}]$ on $\log(g)$ found by Shetrone et al. (2019) for low metallicity stars in APOGEE-DR13 (see also Masseron et al. 2017). We do see moderate trends with $\log(g)$ for $-0.7 \leq [\text{Fe}/\text{H}] \leq -0.5$ when considering the full APOGEE-DR16 disk sample (Fig. 10), consistent with the trend found by Shetrone et al. (2019) at this metallicity. For $Z = 0.004$ ($[\text{Fe}/\text{H}] \approx -0.6$), the Lagarde et al. (2012) models with rotation and thermohaline instability predict a change in $[\text{C}/\text{N}]$ at $\log(g) < 2.0$ that is much larger than observed.

(ix) The predicted $\log(\text{N}/\text{O})$ vs $\log(\text{O}/\text{H}) + 12$ abundance pattern as corrected for mixing in our sample of red giants is in excellent agreement with the gas-phase calibration relation proposed by Dopita et al. (2016) to measure chemical abundances at high-redshift. A good agreement is also obtained with the abundance measurements of Schaefer et al. (2020) in MaNGA galaxies, who assumed the ‘‘R23’’ calibration of Maiolino et al. (2008), whereas the ‘‘ONS’’ calibration of Pilyugin, Vílchez, & Thuan (2010) seems to be disfavoured.

(x) The evolution-corrected $\log(\text{N}/\text{O})$ vs $\log(\text{O}/\text{H}) + 12$ in our sample of red giants is in excellent agreement with the predictions in the simulated star-forming disc galaxies from the cosmological simulation of Vincenzo & Kobayashi (2018a,b); Vincenzo et al. (2019). The simulations do not agree with the mixing-corrected $\log(\text{C}/\text{N})$ ratios, a discrepancy that most likely reflects incorrect C yields.

Our ability to stringently test mixing models is limited by uncertainties in the appropriate choice of birth abundances. However, based on Fig. 6 we conclude that our MESA models with standard mixing are consistent with APOGEE+*Kepler* data to within plausible uncertainties in the birth abundances and calibration uncertainties of the C, N, and O measurements. The mixing-corrected $[\text{C}/\text{N}]$, and $[\text{N}/\text{O}]$ trends in Figs. 7 and 8 and $[\text{C}/\text{Mg}]$ and $[\text{N}/\text{Mg}]$ trends in Fig. 9 therefore provide a reasonable guide to chemical evolution of those elements in the MW disk. The separation of low- α and high- α populations implies that N and (to a lesser degree) C have significant contributions from time-delayed sources, and the $[\text{Fe}/\text{H}]$ trends imply metallicity dependence of N yields. These empirical trends allow new quantitative tests of stellar yield calculations and chemical evolution scenarios.

7 ACKNOWLEDGMENTS

We thank Nadège Lagarde for useful suggestions, and Adam Schaefer for kindly providing the observational data for MaNGA galaxies shown in Fig. 11. This work was supported in part by NSF grant

AST-1909841. FV acknowledges the support of a Fellowship from the Center for Cosmology and AstroParticle Physics at the Ohio State University. DW acknowledges the hospitality of the Institute for Advanced Study and the support of the W.M. Keck Foundation. JM, AM, and SK acknowledge support from the ERC Consolidator Grant funding scheme (project ASTEROCHRONOMETRY, G.A. n. 772293). SH is supported by an NSF Astronomy and Astrophysics Postdoctoral Fellowship under award AST-1801940.

This research has made use of the VizieR catalogue access tool, CDS, Strasbourg, France (DOI : 10.26093/cds/vizie; website: <http://vizier.unistra.fr>). The original description of the VizieR service was published in Ochsenbein, Bauer, & Marcout (2000).

This paper includes data collected by the *Kepler* mission and obtained from the MAST data archive at the Space Telescope Science Institute (STScI). Funding for the *Kepler* mission is provided by the NASA Science Mission Directorate. STScI is operated by the Association of Universities for Research in Astronomy, Inc., under NASA contract NAS 5–26555.

In this work we have made use of SDSS-IV APOGEE-2 DR16 data. Funding for the Sloan Digital Sky Survey IV has been provided by the Alfred P. Sloan Foundation, the U.S. Department of Energy Office of Science, and the Participating Institutions. SDSS-IV acknowledges support and resources from the Center for High-Performance Computing at the University of Utah. The SDSS web site is www.sdss.org.

SDSS-IV is managed by the Astrophysical Research Consortium for the Participating Institutions of the SDSS Collaboration including the Brazilian Participation Group, the Carnegie Institution for Science, Carnegie Mellon University, the Chilean Participation Group, the French Participation Group, Harvard-Smithsonian Center for Astrophysics, Instituto de Astrofísica de Canarias, The Johns Hopkins University, Kavli Institute for the Physics and Mathematics of the Universe (IPMU) / University of Tokyo, the Korean Participation Group, Lawrence Berkeley National Laboratory, Leibniz Institut für Astrophysik Potsdam (AIP), Max-Planck-Institut für Astronomie (MPIA Heidelberg), Max-Planck-Institut für Astrophysik (MPA Garching), Max-Planck-Institut für Extraterrestrische Physik (MPE), National Astronomical Observatories of China, New Mexico State University, New York University, University of Notre Dame, Observatório Nacional / MCTI, The Ohio State University, Pennsylvania State University, Shanghai Astronomical Observatory, United Kingdom Participation Group, Universidad Nacional Autónoma de México, University of Arizona, University of Colorado Boulder, University of Oxford, University of Portsmouth, University of Utah, University of Virginia, University of Washington, University of Wisconsin, Vanderbilt University, and Yale University.

DATA AVAILABILITY

The data underlying this article, including abundances corrected for evolutionary mixing, will be shared on reasonable request to the corresponding author.

REFERENCES

- Afflerbach A., Churchwell E., Werner M. W., 1997, *ApJ*, 478, 190
 Ahumada R., Prieto C. A., Almeida A., Anders F., Anderson S. F., Andrews B. H., Anguiano B., et al., 2020, *ApJS*, 249, 3
 Alloin D., Collin-Souffrin S., Joly M., Vigroux L., 1979, *A&A*, 78, 200

- Amard L., Roquette J., Matt S. P., 2020, *MNRAS*, 499, 3481
- Amorín R., Grazian A., Castellano M., Pentericci L., Fontana A., Sommariva V., van der Wel A., et al., 2014, *ApJL*, 788, L4
- Andrews B. H., Martini P., 2013, *ApJ*, 765, 140
- Andrews B. H., Weinberg D. H., Schönrich R., Johnson J. A., 2017, *ApJ*, 835, 224
- Angelou G. C., Church R. P., Stancliffe R. J., Lattanzio J. C., Smith G. H., 2011, *ApJ*, 728, 79
- Angelou G. C., Stancliffe R. J., Church R. P., Lattanzio J. C., Smith G. H., 2012, *ApJ*, 749, 128
- Angelou G. C., D'Orazi V., Constantino T. N., Church R. P., Stancliffe R. J., Lattanzio J. C., 2015, *MNRAS*, 450, 2423
- Angulo C., Arnould M., Rayet M., Descouvemont P., Baye D., Leclercq-Willain C., Coc A., et al., 1999, *NuPhA*, 656, 3
- Asplund M., Grevesse N., Sauval A. J., Scott P., 2009, *ARA&A*, 47, 481
- Belfiore F., Maiolino R., Tremonti C., Sánchez S. F., Bundy K., Bershady M., Westfall K., et al., 2017, *MNRAS*, 469, 151
- Bellardini M. A., Wetzel A., Loebman S. R., Faucher-Giguère C.-A., Ma X., Feldmann R., 2021, preprint (arXiv:2102.06220)
- Berg D. A., Skillman E. D., Marble A. R., van Zee L., Engelbracht C. W., Lee J. C., Kennicutt R. C., et al., 2012, *ApJ*, 754, 98
- Berg D. A., Pogge R. W., Skillman E. D., Croxall K. V., Moustakas J., Rogers N. S. J., Sun J., 2020, *ApJ*, 893, 96
- Bird J. C., Kazantzidis S., Weinberg D. H., 2012, *MNRAS*, 420, 913
- Blanc G. A., Kewley L., Vogt F. P. A., Dopita M. A., 2015, *ApJ*, 798, 99
- Böhm-Vitense E., 1958, *ZA*, 46, 108
- Borucki W. J., Koch D., Basri G., Batalha N., Brown T., Caldwell D., Caldwell J., et al., 2010, *Sci*, 327, 977
- Bossini D., Miglio A., Salaris M., Pietrinferni A., Montalbán J., Bressan A., Noels A., et al., 2015, *MNRAS*, 453, 2290
- Bundy K., Bershady M. A., Law D. R., Yan R., Drory N., MacDonald N., Wake D. A., et al., 2015, *ApJ*, 798, 7
- Cantiello M., Langer N., 2010, *A&A*, 521, A9
- Casagrande L., Silva Aguirre V., Schlesinger K. J., Stello D., Huber D., Serenelli A. M., Schönrich R., et al., 2016, *MNRAS*, 455, 987
- Casali G., Magrini L., Tognelli E., Jackson R., Jeffries R. D., Lagarde N., Tautvaišienė G., et al., 2019, *A&A*, 629, A62
- Chaboyer B., Zahn J.-P., 1992, *A&A*, 253, 173
- Chaboyer B., Demarque P., Pinsonneault M. H., 1995, *ApJ*, 441, 865
- Charbonnel C., Vauclair S., Zahn J.-P., 1992, *A&A*, 255, 191
- Charbonnel C., 1995, *ApJL*, 453, L41
- Charbonnel C., Zahn J.-P., 2007, *A&A*, 467, L15
- Charbonnel C., Lagarde N., 2010, *A&A*, 522, A10
- Chiappini C., Romano D., Matteucci F., 2003, *MNRAS*, 339, 63
- Chiappini C., Matteucci F., Ballero S. K., 2005, *A&A*, 437, 429
- Constantino T., Campbell S. W., Christensen-Dalsgaard J., Lattanzio J. C., Stello D., 2015, *MNRAS*, 452, 123
- Constantino T., Campbell S. W., Lattanzio J. C., van Duijneveldt A., 2016, *MNRAS*, 456, 3866
- Constantino T., Campbell S. W., Lattanzio J. C., 2017, *MNRAS*, 472, 4900
- Cottrell P. L., Sneden C., 1986, *A&A*, 161, 314
- Curti M., Maiolino R., Cirasuolo M., Mannucci F., Williams R. J., Auger M., Mercurio A., et al., 2020, *MNRAS*, 492, 821
- da Silva L., Girardi L., Pasquini L., Setiawan J., von der Lühse O., de Medeiros J. R., Hatzes A., et al., 2006, *A&A*, 458, 609
- Dearborn D. S. P., Eggleton P. P., Schramm D. N., 1976, *ApJ*, 203, 455
- Dearborn D. S. P., Tinsley B. M., Schramm D. N., 1978, *ApJ*, 223, 557
- Decressin T., Mathis S., Palacios A., Siess L., Talon S., Charbonnel C., Zahn J.-P., 2009, *A&A*, 495, 271
- Decressin T., Charbonnel C., Siess L., Palacios A., Meynet G., Georgy C., 2009, *A&A*, 505, 727
- Denicoló G., Terlevich R., Terlevich E., 2002, *MNRAS*, 330, 69
- Denissenkov P. A., 2010, *ApJ*, 723, 563
- Denissenkov P. A., Merryfield W. J., 2011, *ApJL*, 727, L8
- Dopita M. A., Kewley L. J., Sutherland R. S., Nicholls D. C., 2016, *Ap&SS*, 361, 61
- Dotter A., Conroy C., Cargile P., Asplund M., 2017, *ApJ*, 840, 99
- Eggleton P. P., Dearborn D. S. P., Lattanzio J. C., 2006, *Sci*, 314, 1580
- Elsworth Y., Hekker S., Johnson J. A., Kallinger T., Mosser B., Pinsonneault M., Hon M., et al., 2019, *MNRAS*, 489, 4641
- Esteban C., García-Rojas J., 2018, *MNRAS*, 478, 2315. doi:10.1093/mnras/sty1168
- Esteban C., Bresolin F., García-Rojas J., Toribio San Cipriano L., 2020, *MNRAS*, 491, 2137
- Ferguson J. W., Alexander D. R., Allard F., Barman T., Bodnarik J. G., Hauschildt P. H., Heffner-Wong A., et al., 2005, *ApJ*, 623, 585
- Fernández-Martín A., Pérez-Montero E., Vílchez J. M., Mampaso A., 2017, *A&A*, 597, A84
- Freeman K., Bland-Hawthorn J., 2002, *ARA&A*, 40, 487
- Feuillet D. K., Bovy J., Holtzman J., Weinberg D. H., García-Hernández D., Hearty F. R., Majewski S. R., et al., 2018, *MNRAS*, 477, 2326
- Garaud P., 2021, preprint (arXiv:2103.08072)
- Gardner J. P., Mather J. C., Clampin M., Doyon R., Greenhouse M. A., Hammel H. B., Hutchings J. B., et al., 2006, *SSRv*, 123, 485
- Garnett D. R., Shields G. A., 1987, *ApJ*, 317, 82
- Gilmore G., Randich S., Asplund M., Binney J., Bonifacio P., Drew J., Feltzing S., et al., 2012, *Msngr*, 147, 25
- Gilroy K. K., 1989, *ApJ*, 347, 835
- Gratton R. G., Sneden C., Carretta E., Bragaglia A., 2000, *A&A*, 354, 169
- Greene T. F., 1969, *ApJ*, 157, 737
- Grevesse N., Asplund M., Sauval A. J., 2007, *SSRv*, 130, 105. doi:10.1007/s11214-007-9173-7
- Grieves N., Ge J., Thomas N., Willis K., Ma B., Lorenzo-Oliveira D., Queiroz A. B. A., et al., 2018, *MNRAS*, 481, 3244
- Griffith E., Johnson J. A., Weinberg D. H., 2019, *ApJ*, 886, 84
- Griffith E. J., Sukhbold T., Weinberg D. H., Johnson J. A., Johnson J. W., Vincenzo F., 2021, preprint (arXiv:2103.09837)
- Hayden M. R., Bovy J., Holtzman J. A., Nidever D. L., Bird J. C., Weinberg D. H., Andrews B. H., et al., 2015, *ApJ*, 808, 132
- Henry R. B. C., Edmunds M. G., Köppen J., 2000, *ApJ*, 541, 660
- Herwig F., Bloeker T., Schoenberner D., El Eid M., 1997, *A&A*, 324, L81
- Holtzman J. A., Hasselquist S., Shetrone M., Cunha K., Allende Prieto C., Anguiano B., Bizyaev D., et al., 2018, *AJ*, 156, 125
- Iben I., 1964, *ApJ*, 140, 1631
- Iben I., 1967, *ApJ*, 147, 624
- Iben I., 1968, *Natur*, 220, 143. doi:10.1038/220143a0
- Iglesias C. A., Rogers F. J., 1996, *ApJ*, 464, 943
- Irwin A. W., 2012, (ascl:1211.002)
- Izotov Y. I., Thuan T. X., Guseva N. G., 2012, *A&A*, 546, A122
- James B. L., Koposov S., Stark D. P., Belokurov V., Pettini M., Olszewski E. W., 2015, *MNRAS*, 448, 2687
- Jönsson H., Allende Prieto C., Holtzman J. A., Feuillet D. K., Hawkins K., Cunha K., Mészáros S., et al., 2018, *AJ*, 156, 126
- Jönsson H., Holtzman J. A., Allende Prieto C., Cunha K., García-Hernández D. A., Hasselquist S., Masseron T., et al., 2020, *AJ*, 160, 120
- Johnson J. W., Weinberg D. H., 2020, *MNRAS*, 498, 1364
- Johnson J. W., Weinberg D. H., Vincenzo F., Bird J. C., Loebman S. R., Brooks A. M., Quinn T. R., et al., 2021, preprint (arXiv:2103.09838)
- Khan S., Hall O. J., Miglio A., Davies G. R., Mosser B., Girardi L., Montalbán J., 2018, *ApJ*, 859, 156
- Kewley L. J., Dopita M. A., 2002, *ApJS*, 142, 35
- Kewley L. J., Ellison S. L., 2008, *ApJ*, 681, 1183
- Kjaergaard P., Gustafsson B., Walker G. A. H., Hultqvist L., 1982, *A&A*, 115, 145
- Korn A. J., Grundahl F., Richard O., Mashonkina L., Barklem P. S., Collet R., Gustafsson B., et al., 2007, *ApJ*, 671, 402
- Kobayashi C., Umeda H., Nomoto K., Tominaga N., Ohkubo T., 2006, *ApJ*, 653, 1145
- Kobayashi C., Karakas A. I., Lugaro M., 2020, *ApJ*, 900, 179
- Lagarde N., Decressin T., Charbonnel C., Eggenberger P., Ekström S., Palacios A., 2012, *A&A*, 543, A108
- Lagarde N., Reylé C., Robin A. C., Tautvaišienė G., Drazdauskas A., Mikolaitis Š., Minkevičiūtė R., et al., 2019, *A&A*, 621, A24
- Lambert D. L., Ries L. M., 1977, *ApJ*, 217, 508
- Lind K., Korn A. J., Barklem P. S., Grundahl F., 2008, *A&A*, 490, 777

- Loebman S. R., Roškar R., Debattista V. P., Ivezić Ž., Quinn T. R., Wadsley J., 2011, *ApJ*, 737, 8
- López-Sánchez Á. R., Dopita M. A., Kewley L. J., Zahid H. J., Nicholls D. C., Scharwächter J., 2012, *MNRAS*, 426, 2630
- Maeder A., Zahn J.-P., 1998, *A&A*, 334, 1000
- Magrini L., Vincenzo F., Randich S., Pancino E., Casali G., Tautvaišienė G., Drazdauskas A., et al., 2018, *A&A*, 618, A102
- Majewski S. R., Schiavon R. P., Frinchaboy P. M., Allende Prieto C., Barkhouser R., Bizyaev D., Blank B., et al., 2017, *AJ*, 154, 94
- Maiolino R., Nagao T., Grazian A., Cocchia F., Marconi A., Mannucci F., Cimatti A., et al., 2008, *A&A*, 488, 463
- Martig M., Fouesneau M., Rix H.-W., Ness M., Mészáros S., García-Hernández D. A., Pinsonneault M., et al., 2016, *MNRAS*, 456, 3655
- Masseron T., Gilmore G., 2015, *MNRAS*, 453, 1855
- Masseron T., Lagarde N., Miglio A., Elsworth Y., Gilmore G., 2017, *MNRAS*, 464, 3021
- Matteucci F., 1986, *MNRAS*, 221, 911
- Miglio A., Chiappini C., Mackereth J. T., Davies G. R., Brogaard K., Casagrande L., Chaplin W. J., et al., 2021, *A&A*, 645, A85
- Minchev I., Chiappini C., Martig M., 2013, *A&A*, 558, A9
- Minchev I., Chiappini C., Martig M., 2014, *A&A*, 572, A92
- Mollá M., Cavichia O., Gavilán M., Gibson B. K., 2015, *MNRAS*, 451, 3693
- Montalbán J., Kupka F., D'Antona F., Schmidt W., 2001, *A&A*, 370, 982
- Montalbán J., D'Antona F., Kupka F., Heiter U., 2004, *A&A*, 416, 1081. doi:10.1051/0004-6361:20031728
- Morel P., Thévenin F., 2002, *A&A*, 390, 611
- Moustakas J., Kennicutt R. C., Tremonti C. A., Dale D. A., Smith J.-D. T., Calzetti D., 2010, *ApJS*, 190, 233
- Ness M., Hogg D. W., Rix H.-W., Martig M., Pinsonneault M. H., Ho A. Y. Q., 2016, *ApJ*, 823, 114
- Nieva M.-F., Przybilla N., 2012, *A&A*, 539, A143
- Ochsenbein F., Bauer P., Marcout J., 2000, *A&AS*, 143, 23
- Pagel B. E. J., Edmunds M. G., Blackwell D. E., Chun M. S., Smith G., 1979, *MNRAS*, 189, 95
- Pagel B. E. J., Edmunds M. G., 1981, *ARA&A*, 19, 77
- Palacios A., Talon S., Charbonnel C., Forestini M., 2003, *A&A*, 399, 603
- Palacios A., Charbonnel C., Talon S., Siess L., 2006, *A&A*, 453, 261
- Paxton B., Bildsten L., Dotter A., Herwig F., Lesaffre P., Timmes F., 2011, *ApJS*, 192, 3
- Paxton B., Cantiello M., Arras P., Bildsten L., Brown E. F., Dotter A., Mankovich C., et al., 2013, *ApJS*, 208, 4
- Paxton B., Marchant P., Schwab J., Bauer E. B., Bildsten L., Cantiello M., Dessart L., et al., 2015, *ApJS*, 220, 15
- Paxton B., Schwab J., Bauer E. B., Bildsten L., Blinnikov S., Duffell P., Farmer R., et al., 2018, *ApJS*, 234, 34
- Pérez-Montero E., Contini T., 2009, *MNRAS*, 398, 949
- Pérez-Montero E., García-Benito R., Vílchez J. M., Sánchez S. F., Kehrig C., Husemann B., Duarte Puertas S., et al., 2016, *A&A*, 595, A62
- Pettini M., Ellison S. L., Bergeron J., Petitjean P., 2002, *A&A*, 391, 21
- Pettini M., Pagel B. E. J., 2004, *MNRAS*, 348, L59
- Pettini M., Zych B. J., Steidel C. C., Chaffee F. H., 2008, *MNRAS*, 385, 2011
- Pilyugin L. S., Vílchez J. M., Thuan T. X., 2010, *ApJ*, 720, 1738
- Pinsonneault M. H., Elsworth Y. P., Tayar J., Serenelli A., Stello D., Zinn J., Mathur S., et al., 2018, *ApJS*, 239, 32
- Portinari L., Chiosi C., 2000, *A&A*, 355, 929
- Prantzos N., Abia C., Limongi M., Chieffi A., Cristallo S., 2018, *MNRAS*, 476, 3432
- Randich S., Gilmore G., Gaia-ESO Consortium, 2013, *Msngr*, 154, 47
- Rodrigues T. S., Girardi L., Miglio A., Bossini D., Bovy J., Epstein C., Pinsonneault M. H., et al., 2014, *MNRAS*, 445, 2758
- Rodrigues T. S., Bossini D., Miglio A., Girardi L., Montalbán J., Noels A., Trabucchi M., et al., 2017, *MNRAS*, 467, 1433
- Romano D., Karakas A. I., Tosi M., Matteucci F., 2010, *A&A*, 522, A32
- Rudolph A. L., Fich M., Bell G. R., Norsen T., Simpson J. P., Haas M. R., Erickson E. F., 2006, *ApJS*, 162, 346
- Rybizki J., Just A., Rix H.-W., 2017, *A&A*, 605, A59
- Salaris M., Cassisi S., Weiss A., 2002, *PASP*, 114, 375
- Salaris M., Pietrinferni A., Piersimoni A. M., Cassisi S., 2015, *A&A*, 583, A87
- Sánchez S. F., Kennicutt R. C., Gil de Paz A., van de Ven G., Vílchez J. M., Wisotzki L., Walcher C. J., et al., 2012, *A&A*, 538, A8
- Schaefer A. L., Tremonti C., Belfiore F., Pace Z., Bershady M. A., Andrews B. H., Drory N., 2020, *ApJL*, 890, L3
- Shaver P. A., McGee R. X., Newton L. M., Danks A. C., Pottasch S. R., 1983, *MNRAS*, 204, 53
- Schönrich R., Binney J., 2009, *MNRAS*, 396, 203
- Schwarzschild M., 1958, Princeton, Princeton University Press
- Shetrone M. D., Sneden C., Pilachowski C. A., 1993, *PASP*, 105, 337
- Shetrone M., Tayar J., Johnson J. A., Somers G., Pinsonneault M. H., Holtzman J. A., Hasselquist S., et al., 2019, *ApJ*, 872, 137
- Siess L., Dufour E., Forestini M., 2000, *A&A*, 358, 593
- Smith G. H., Tout C. A., 1992, *MNRAS*, 256, 449
- Spite M., Cayrel R., Plez B., Hill V., Spite F., Depagne E., François P., et al., 2005, *A&A*, 430, 655
- Stancliffe R. J., Fossati L., Passy J.-C., Schneider F. R. N., 2016, *A&A*, 586, A119
- Steidel C. C., Rudie G. C., Strom A. L., Pettini M., Reddy N. A., Shapley A. E., Trainor R. F., et al., 2014, *ApJ*, 795, 165
- Souto D., Cunha K., Smith V. V., Allende Prieto C., García-Hernández D. A., Pinsonneault M., Holzer P., et al., 2018, *ApJ*, 857, 14
- Souto D., Allende Prieto C., Cunha K., Pinsonneault M., Smith V. V., Garcia-Dias R., Bovy J., et al., 2019, *ApJ*, 874, 97
- Tautvaišienė G., Edvardsson B., Puzeras E., Barisevičius G., Ilyin I., 2010, *MNRAS*, 409, 1213
- Thomas H.-C., 1967, *ZA*, 67, 420
- Thoul A. A., Bahcall J. N., Loeb A., 1994, *ApJ*, 421, 828
- Vílchez J. M., Esteban C., 1996, *MNRAS*, 280, 720
- Vincenzo F., Belfiore F., Maiolino R., Matteucci F., Ventura P., 2016, *MNRAS*, 458, 3466
- Vincenzo F., Kobayashi C., 2018, *A&A*, 610, L16
- Vincenzo F., Kobayashi C., 2018, *MNRAS*, 478, 155
- Vincenzo F., Miglio A., Kobayashi C., Mackereth J. T., Montalbán J., 2019, *A&A*, 630, A125
- Vincenzo F., Kobayashi C., 2020, *MNRAS*, 496, 80
- Vincenzo F., Weinberg D. H., Miglio A., Lane R. R., Roman-Lopes A., 2021, preprint (arXiv:2101.04488)
- Weinberg D. H., Holtzman J. A., Hasselquist S., Bird J. C., Johnson J. A., Shetrone M., Sobeck J., et al., 2019, *ApJ*, 874, 102
- Wilson J. C., Hearty F. R., Skrutskie M. F., Majewski S. R., Holtzman J. A., Eisenstein D., Gunn J., et al., 2019, *PASP*, 131, 055001
- Zahn J.-P., 1992, *A&A*, 265, 115